nature sustainability

Supplementary information https://doi.org/10.1038/s41893-026-01859-y

Global patterns of reservoir sedimentation and overlooked risks in small reservoirs

In the format provided by the authors and unedited

Table of Contents

The file includes:

Supplementary Text S1. Data harmonization and quality control procedures

Supplemental datasets may contain inaccuracies such as false dam entries, mislocated damming points (e.g., outside mapped water extents), and reservoirs that are dried or no longer operational. To address these issues, we implemented a manual inspection process by overlaying all collected reservoir and dam locations onto high-resolution satellite imagery. This quality-control procedure included two rounds of validation to ensure spatial accuracy and reliability.

Geometric consistency was ensured by standardizing all datasets to the WGS84 geographic coordinate system. To maintain semantic consistency among datasets, a standardized protocol was applied to harmonize reservoir attributes such as name, area, and storage capacity. Cross-checks between spatial locations and attribute fields were conducted to identify and remove redundant or duplicate records. When duplicate entries existed, priority was given to records containing more complete attribute information.

Attribute inconsistencies across datasets were resolved using a rule-based protocol. A source-priority hierarchy was adopted in which peer-reviewed global inventories were used as primary references, while validated national datasets were used to update attribute information when inconsistencies occurred. Attribute values with clear definitions and explicit units were retained, whereas implausible or unverifiable entries were excluded.

Supplementary Text S2. Topology correction and quality control procedures

Quality-control procedures were implemented to ensure geometric and spatial consistency of reservoir boundaries (Supplementary Fig. 13). First, spatial topological errors, such as overlapping and self-intersecting polygons and erroneously merged adjacent reservoirs, presented significant obstacles. Second, the delineation of reservoir boundaries was further complicated by their frequent overlap with complex terrains such as floodplains and river terraces. To resolve these issues, we utilized high-resolution satellite imagery from ESRI World Imagery, performing manual vector editing and boundary clipping to refine and optimize reservoir boundaries and ensure spatial integrity. Additionally, mismatches between reservoir attributes and spatial geometry (e.g., discrepancies in area or location) were identified and corrected to prevent misclassification. To enhance the accuracy and reliability of the reservoir boundary data, a second phase of multi-level quality control was conducted by four graduate students over a one-month period.

Supplementary Text S3. Estimation of reservoir construction year and attribute completion

The construction year is an important attribute for analyzing the spatiotemporal evolution of reservoirs. To reconstruct comprehensive reservoir construction years, we developed a hierarchical strategy that integrates archival records, multi-temporal remote sensing analysis, and national-scale statistical attribution (Supplementary Fig. 15). Initially, we consolidated explicit construction years for 104,958 reservoirs from existing inventories to serve as ground truth. For the remaining reservoirs, we employed a retrospective analysis using the GSW dataset by synthesizing maximum water extents across the four epochs of 1984–1989, 1990–1999, 2000–2010, and 2010–2020. Guided by empirical calibration using reservoirs of known age, we established a stepwise identification approach based on water surface stability. We defined a threshold of 20% for the area expansion ratio to classify reservoirs sequentially. First, reservoirs were classified as pre-1990 (n = 213,299) if the proportion of new water surface emerging between 1990 and 2020 was ≤ 20% of their maximum extent (1984-2020), suggesting the reservoir was already established before the 1984–1989 baseline. Second, for reservoirs constructed post-1990, we determined the timing based on relative stability in subsequent periods. Reservoirs were assigned to the 1990–2000 interval (1995 ± 5 years, n = 55,426) if the new water area added in 2000–2020 was ≤ 20% relative to the 1990–2000 extent. Similarly, reservoirs were classified into the 2000–2010 interval (2005 ± 5 years, n = 41,335) if the new area added in 2010–2020 was ≤ 20% relative to the 2000–2010 extent. The remaining reservoirs showing significant expansion (>20%) were categorized into 2010–2020 (2015 ± 5 years, n = 22,790). To corroborate the robustness of this remote sensing approach, we performed a systematic visual inspection of 13,999 samples across six randomly selected 5° × 5° grids using high-resolution Google Earth historical imagery, which yielded classification accuracy exceeding 99% across all regions.

For the reservoirs identified as pre-1990, and the 118,152 reservoirs where construction intervals remained undetermined due to size limitations or signal noise, we applied a statistical attribution approach based on the premise that dam construction is driven by national sociopolitical and economic development phases. Specifically, for the pre-1990 group, we utilized the mean construction year of all known pre-1990 reservoirs within the respective country. For the remaining undetermined reservoirs, we assigned the mean construction year of all documented reservoirs in that country. In both scenarios, the standard deviation of the national records was calculated and retained to quantify the methodological uncertainty. Other attributes such as dam height and reservoir name were extracted by integrating publicly available datasets (e.g., GRanD and GeoDAR) with supplementary online searches.

Supplementary Text S4. Predictor variable preprocessing

Predictor variables were derived from a range of data sources, including reservoir extent measurements, satellite remote sensing-based estimations, atmospheric and hydrological reanalysis data, soil and lithological maps, and digital elevation models. For time-sensitive variables, such as precipitation, runoff, and nighttime light, we synthesized long-term average values to improve the robustness of sedimentation predictions. For variables available from 1980 or earlier (e.g., precipitation, temperature), averages from 1980 to 2020 were calculated. For those starting after 1980 (e.g., nighttime lights data from 1992–2020), data from the earliest available year were used. This 40-year timespan was chosen because Earth observation technologies have improved data accuracy significantly since the 1980s, and 87.4% of our sedimentation samples were surveyed after 1980. Using the post-1980 averages may reach a balance between data accuracy and temporal alignment with the sample data. To ensure consistency and compatibility, all spatial variables were resampled to a standardized 90-meter resolution for analysis (Supplementary Figs. 17–22). Detailed descriptions of these variables, including their categories, data sources, time spans, and spatial resolution, are provided in Supplementary Table 11.

Supplementary Text S5. Importance analysis of different driving variables

In this study, we compiled a comprehensive set of variables to predict reservoir mean depth and sedimentation rate. To identify the most significant contributors to model predictions, we performed a variable importance analysis using Gini importance and SHAP (SHapley Additive exPlanations) values. Gini importance, or "mean decrease in impurity" (MDI), quantifies the importance of variables in tree-based models. It evaluates the reduction in impurity (e.g., Gini impurity or entropy) achieved by splitting on a particular feature across all trees in the ensemble. While effective and interpretable, Gini importance has a known bias, often assigning higher importance scores to features with more categories or continuous variables. To complement this, we employed SHAP values, which attribute the contribution of each feature to a specific prediction. SHAP values are widely recognized for providing detailed, instance-level explanations and ensuring a fair distribution of contributions among features. By combining insights from both Gini importance and SHAP values, we uncovered hidden drivers influencing the spatial patterns of global reservoir sedimentation rates, thereby enhancing both the interpretability and reliability of our model predictions. To further quantify the influence of different dimensions of predictors on model behavior, we grouped the 49 predictor variables into seven thematic categories: climate, soil, geomorphology, hydrology, land cover, human activity, and reservoir location and morphology. This grouping enables quantitative assessment of relative importance and contributing at both the individual-variable and broader process levels. Furthermore, to explore the spatial importance of different drivers, we applied the SHAP-based importance analysis to model predictions across a global 5° × 5° grid. Within each grid cell, SHAP values were aggregated to identify the top contributing variable groups, allowing us to capture regional differences in sedimentation mechanisms and reveal spatial heterogeneity in sedimentation controls.

Supplementary Text S6. Influence of variable combination and training samples selection

To enhance the robustness of the developed sedimentation prediction model, we conducted comparative analyses on the influence of diverse combinations of contributing variables, various subsampling strategies, and modeling spatial scales (Supplementary Table 12). This process supported the selection of an optimal model to ensure high accuracy and reliability of global-scale predictions. By calculating variable importance, we identified the top 10, 15, and 20 variables ranked by SHAP values and constructed predictive models based on these subsets to evaluate if variable selection could improve accuracy. The results indicated a slight decrease in model estimation accuracy after variable selection (Supplementary Table 14), underscoring the importance of incorporating a comprehensive and diverse set of variables for model robustness, particularly given the worldwide variability in reservoir sedimentation.

Another critical consideration was whether the spatial distribution of samples affects model predictive accuracy. In this study, of the 6,133 samples collected, 4,748 originated from China (despite hosting the second largest number of reservoirs in the world), raising concerns about potential spatial bias due to this disproportionately high representation. To assess potential impact of this spatial imbalance, we performed subsampling within the Chinese dataset. Specifically, while retaining all non-Chinese samples, Chinese samples were subsampled at varying ratios (from 1:1 to 1:3). Results show that the model maintained comparable accuracy across all subsampling scenarios, with mean absolute error (MAE) values remaining stable (e.g., 0.38% at 1:4 ratio, 0.34% at 3:1; Supplementary Fig. 25). This suggests that the spatial imbalance does not undermine global model performance, likely because sedimentation variability is more strongly driven by environmental predictors (e.g., climate, soil, and hydrology) than by country of origin.

To further evaluate model generalizability, we implemented a leave-one-country-out cross-validation for 10 major countries, including the USA, India, Brazil, and Australia. In each test, the model was trained on the global dataset excluding one country and then used to predict sedimentation rates for that country. Results show consistently low MAEs (ranging from 0.33% to 0.35%) across all cases (Supplementary Fig. 26), demonstrating robust extrapolation capability across diverse geographic settings. Taken together, these results highlight the resilience of the model to spatial sample imbalances and its strong potential for global application in regions with limited *in-situ* data. In addition, we compared the global model with a national-scale model trained exclusively on Chinese data. The two approaches produced nearly identical estimates of average reservoir sedimentation rates in China (0.51% and 0.53%, respectively), with strong agreement between predictions ($R^2 = 0.65$; Supplementary Fig. 27). This consistency demonstrates that the global model maintains high predictive accuracy even at the national scale. Together, these results confirm that the model not only generalizes well across regions but also performs reliably within individual countries, including those with extensive and heterogeneous reservoir networks.

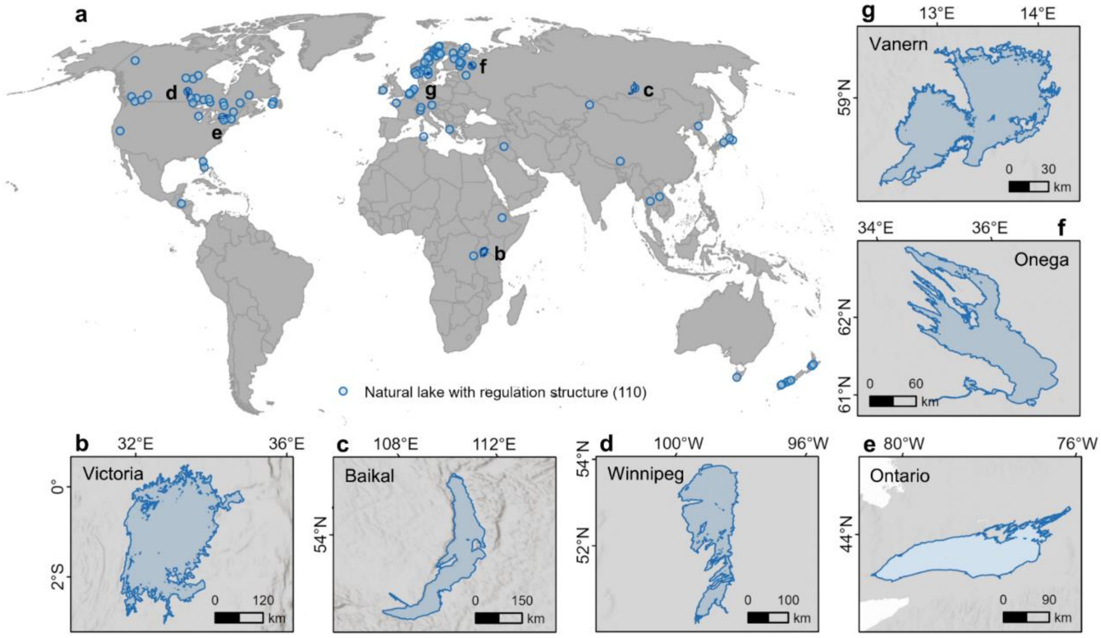

Fig. 1.

The 110 regulated lakes excluded in this study (a) Individual maps show Lake Victoria (b), Lake Baikal (c), Lake Winnipeg (d), Lake Ontario (e), Lake Onega (f), and Lake Vanern (g). During the construction of the GREI dataset, we employed lake data (Type-3) from HydroLAKES as a mask to identify and exclude regulated lakes. These excluded lakes encompass a total surface area of 205,062.40 km^2, with a combined water volume of 626.80 km^3. Basemap: Esri/World Hillshade. Sources: Esri, TomTom, FAO, NOAA, USGS.

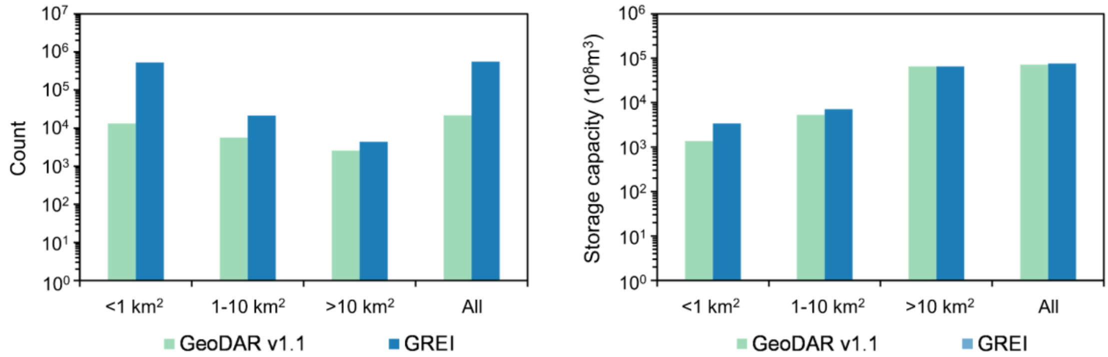

Fig. 2.

Comparison of reservoir counts and storage capacities across different size categories between the GeoDAR v1.1 and GREI datasets. Green bars represent GeoDAR v1.1, while blue bars represent GREI.

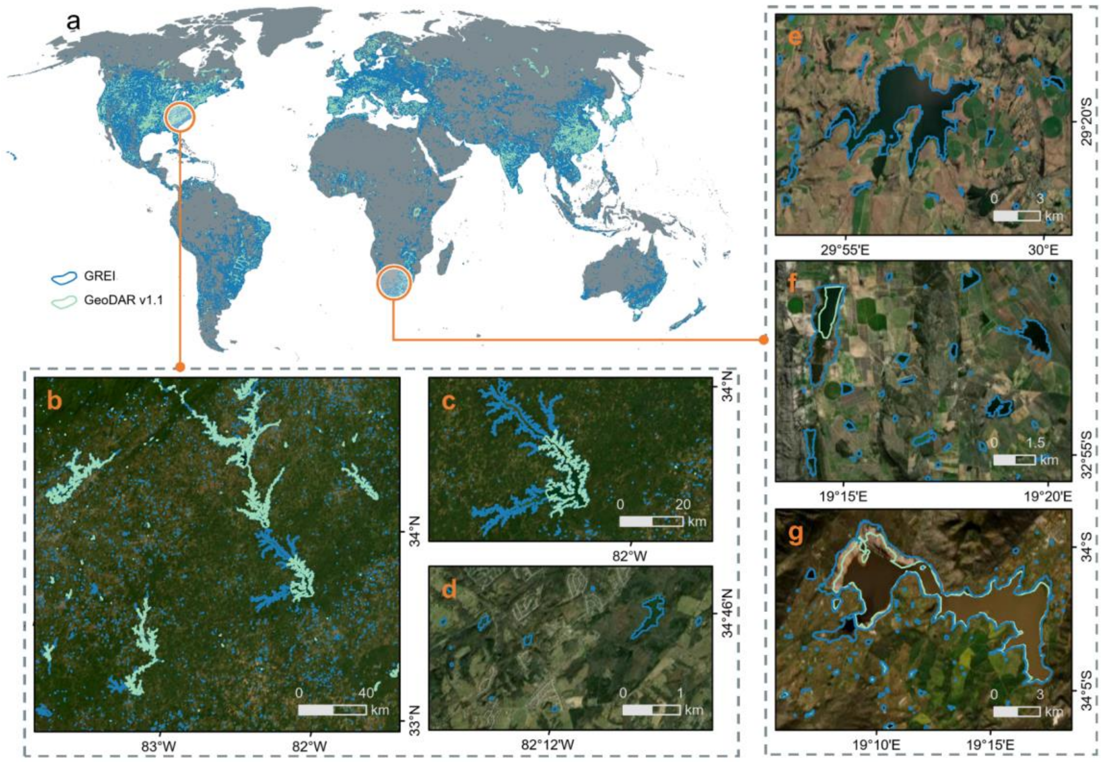

Fig. 3.

Global distribution of reservoirs in both GeoDAR v1.1 and GREI datasets. (a) Regional distributions of reservoirs in both datasets, including the eastern United States (b-d) and southernmost Africa (e-g). Basemap: Esri/World Imagery. Sources: Esri, TomTom, FAO, NOAA, USGS.

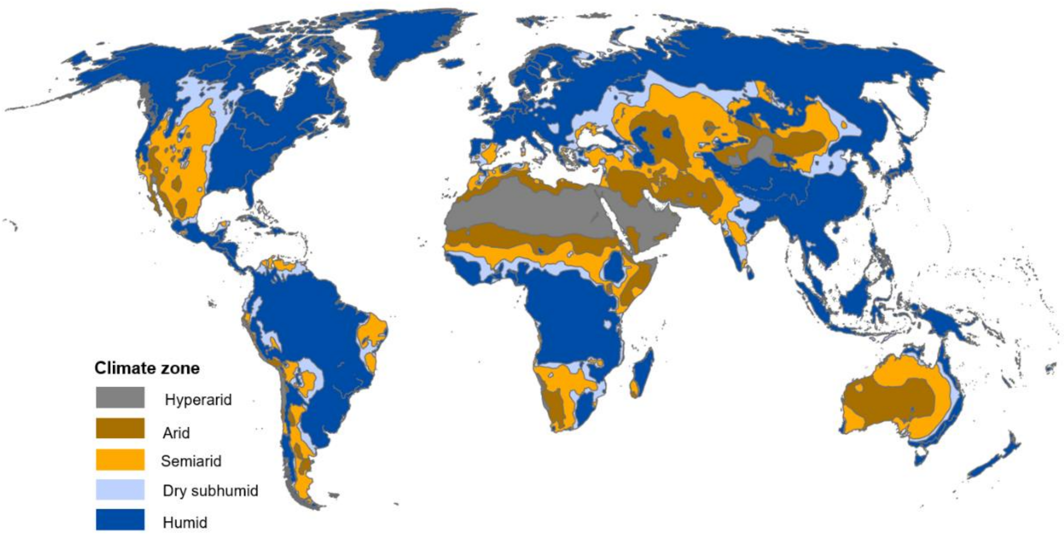

Fig. 4.

Global distribution of climate zones based on aridity classification.

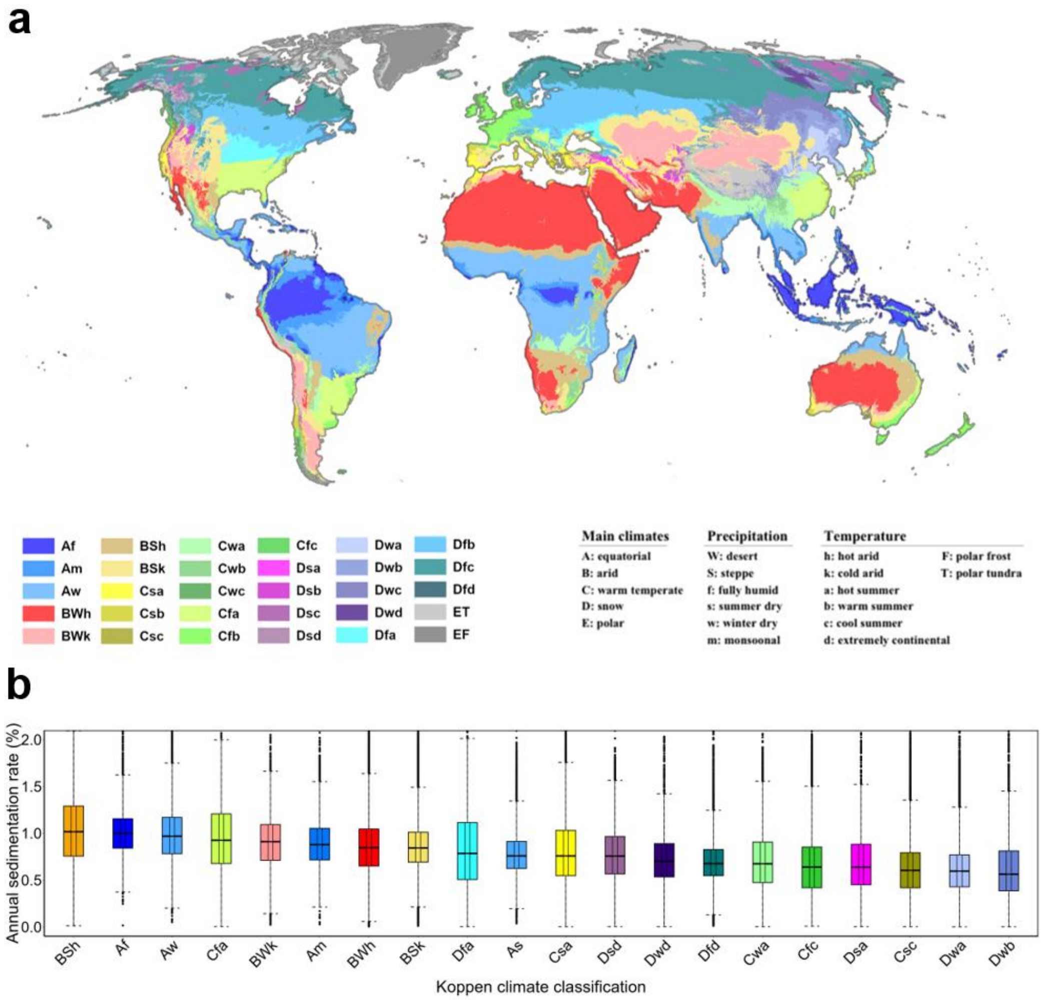

Fig. 5.

Reservoir sedimentation across Köppen climate zones. (a) Map of global Köppen climate classification. (b) Distribution of reservoir sedimentation rates by climate type; categories with fewer than 1,000 reservoirs were excluded. Boxes show the interquartile range (25th–75th percentiles), the center line indicates the median, and points denote outliers.

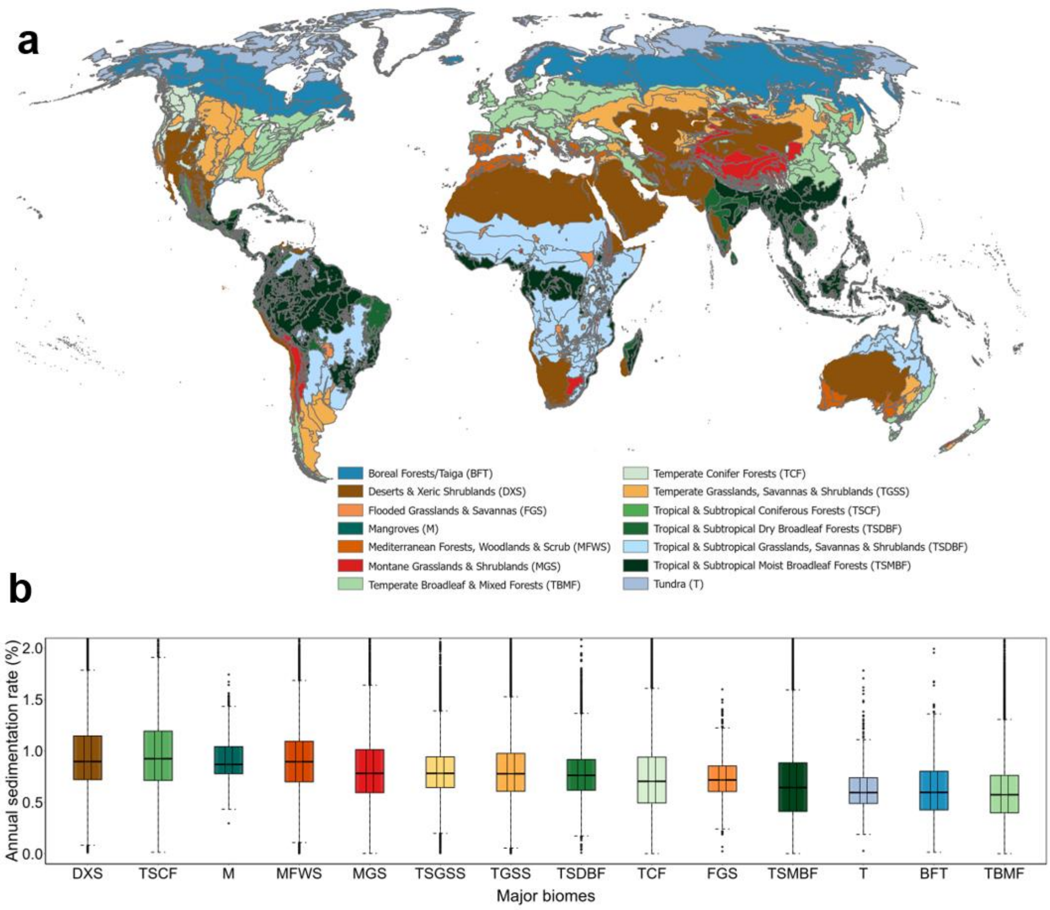

Fig. 6.

Reservoir sedimentation across major biome zones. (a) Map of global biome classification. (b) Distribution of reservoir sedimentation rates by biomes; categories with fewer than 1,000 reservoirs were excluded. Boxes show the interquartile range (25th–75th percentiles), the center line indicates the median, and points denote outliers.

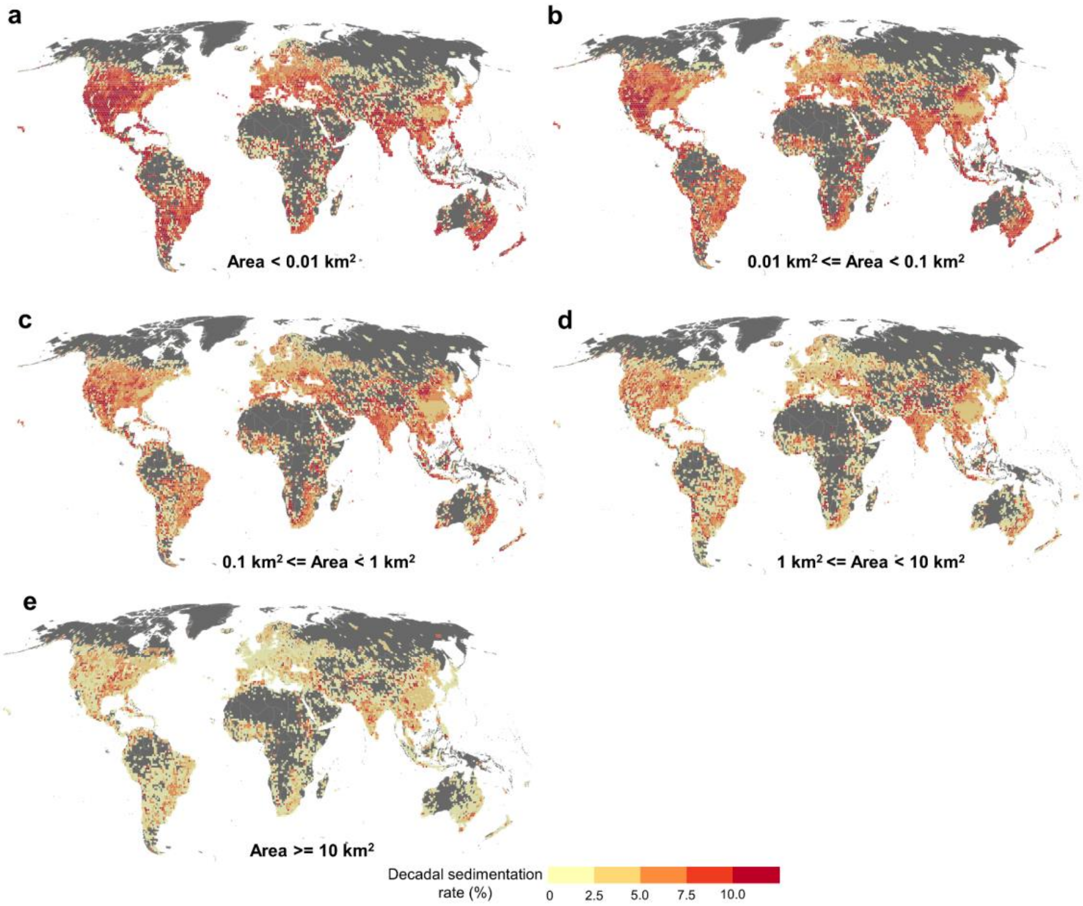

Fig. 7.

Spatial patterns of reservoir sedimentation rates across surface area classes based on 0.1° × 0.1° grid statistics. (a–e) Spatial distribution of decadal sedimentation rates for reservoirs grouped by surface area: < 0.01 km², 0.01–0.1 km², 0.1–1 km², 1–10 km², and ≥ 10 km².

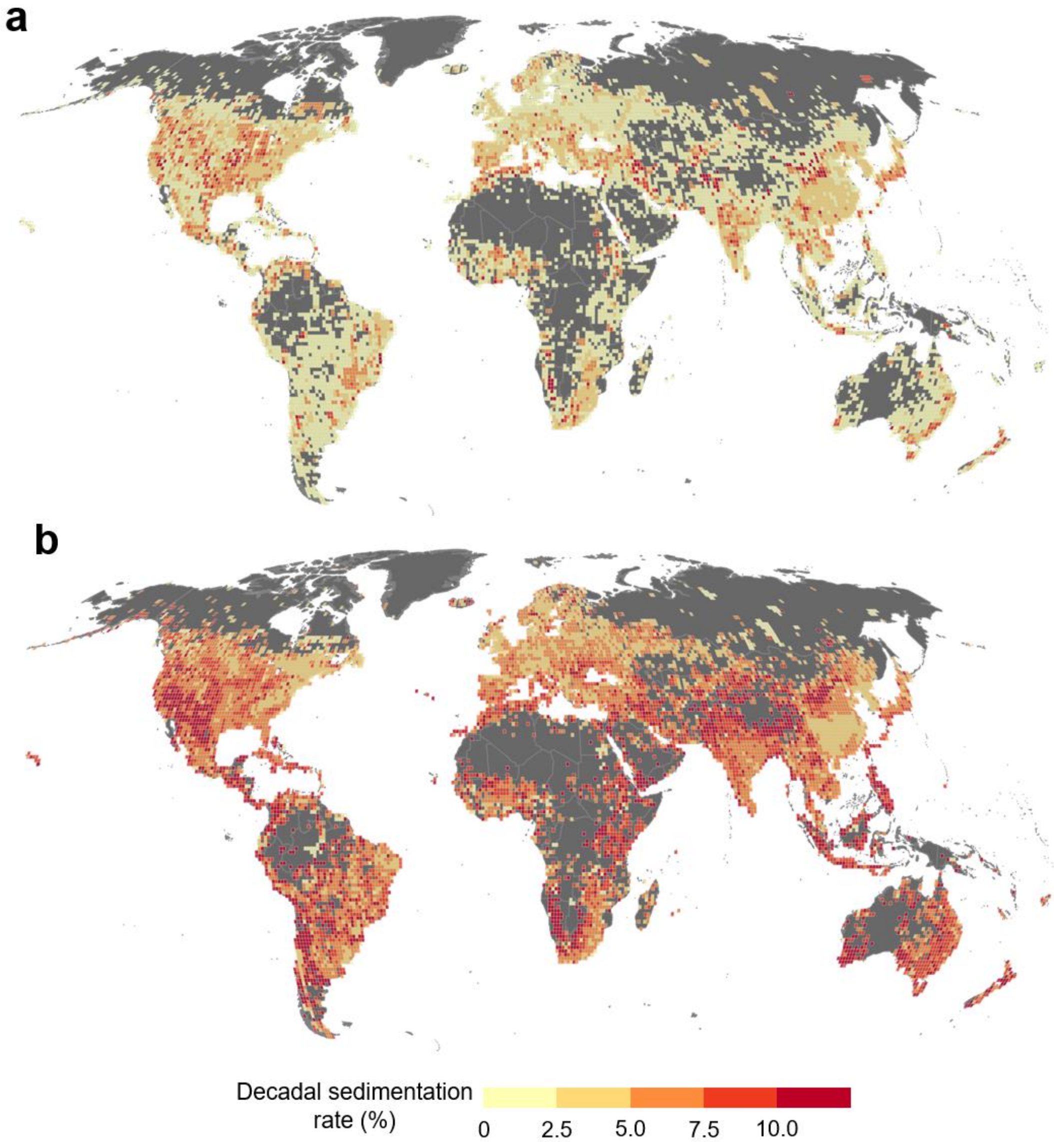

Fig. 8.

Spatial disparities in decadal sedimentation rates derived from the commonly used GRanD dataset and the previously underrepresented small reservoirs included in the GREI. (a) Spatial distribution of decadal sedimentation rates for reservoirs included in the GRanD dataset. (b) Spatial distribution of decadal sedimentation rates for small reservoirs outside the GRanD dataset.

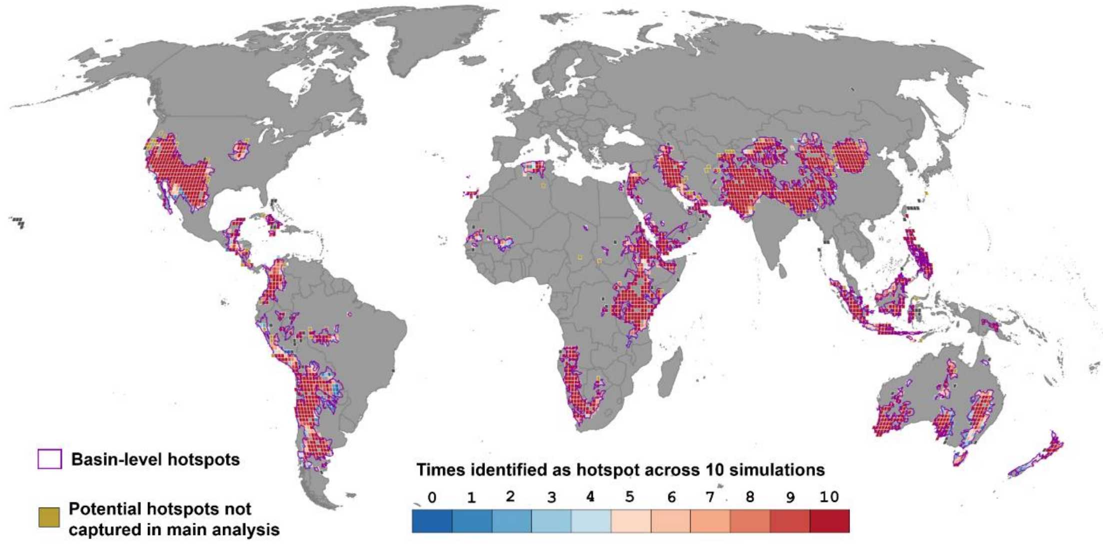

Fig. 9.

Robustness of basin-level sedimentation hotspots under uncertainty. To assess the robustness of global sedimentation hotspot identification, we conducted 10 simulations by perturbing individual reservoir sedimentation rates within their ±1σ uncertainty range. Colored grid cells indicate the number of times each cell was detected as a hotspot across the 10 simulations, reflecting the consistency of hotspot identification. Purple outlines show the basin-level hotspots delineated in the main analysis. Orange cells represent additional grids not included in those basin hotspots but identified as hotspots in more than 5 out of 10 simulations, indicating possible under-detection. Gray cells were detected as hotspots in fewer than 6 simulations and fall outside the original hotspot regions, suggesting lower robustness or peripheral significance.

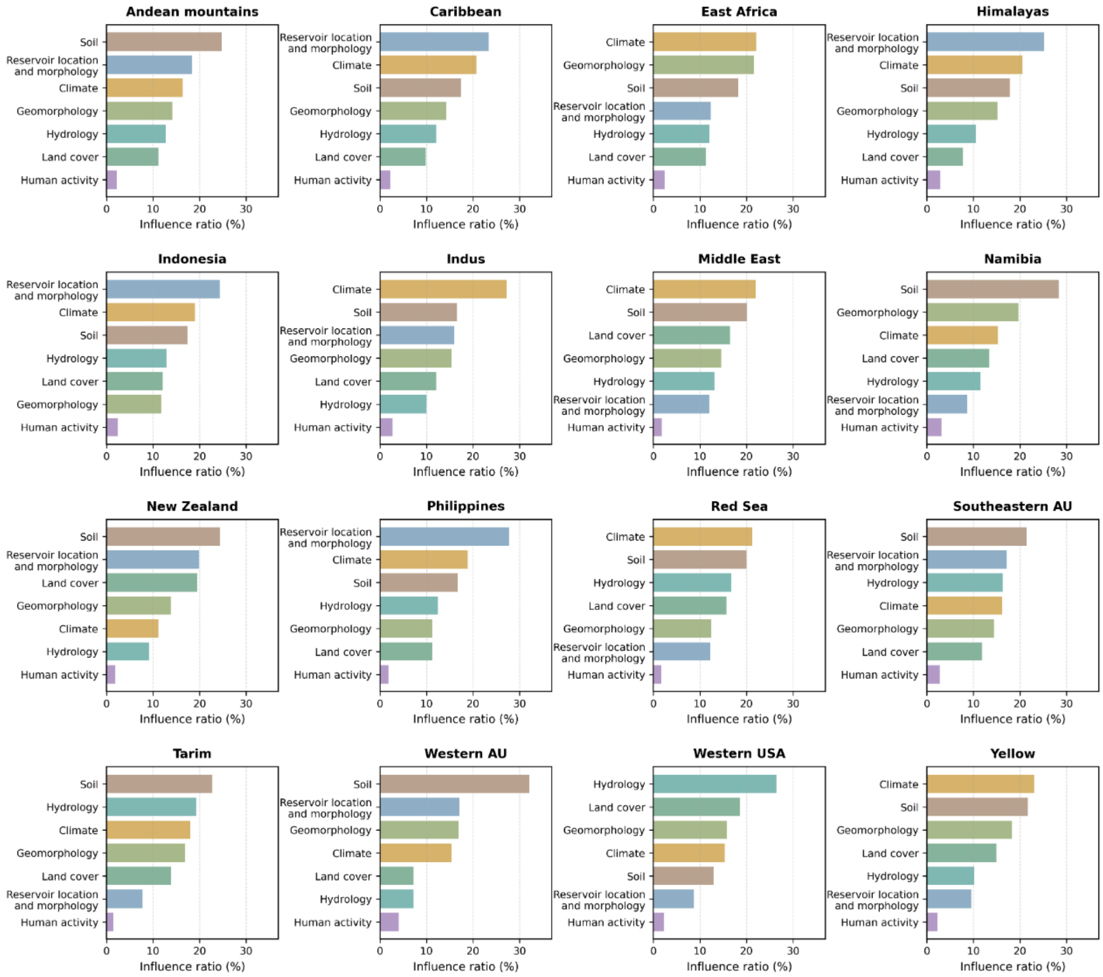

Fig. 10.

SHAP-based analysis of the relative importance of predictor categories across 16 global sedimentation hotspots. Each subplot represents one hotspot region and displays the top seven contributing predictor categories ranked by their SHAP-based influence ratio (%). Overall, soil-related (e.g., texture, erodibility) and climate-related (e.g., precipitation, drought) factors emerge as dominant in 6 and 5 regions, respectively. Hydrology, geomorphology, and reservoir morphology also show strong influence in several areas. The regional variation in dominant drivers underscores the capacity of the model to adaptively capture location-specific sedimentation mechanisms, highlighting its robustness and generalizability at a global scale.

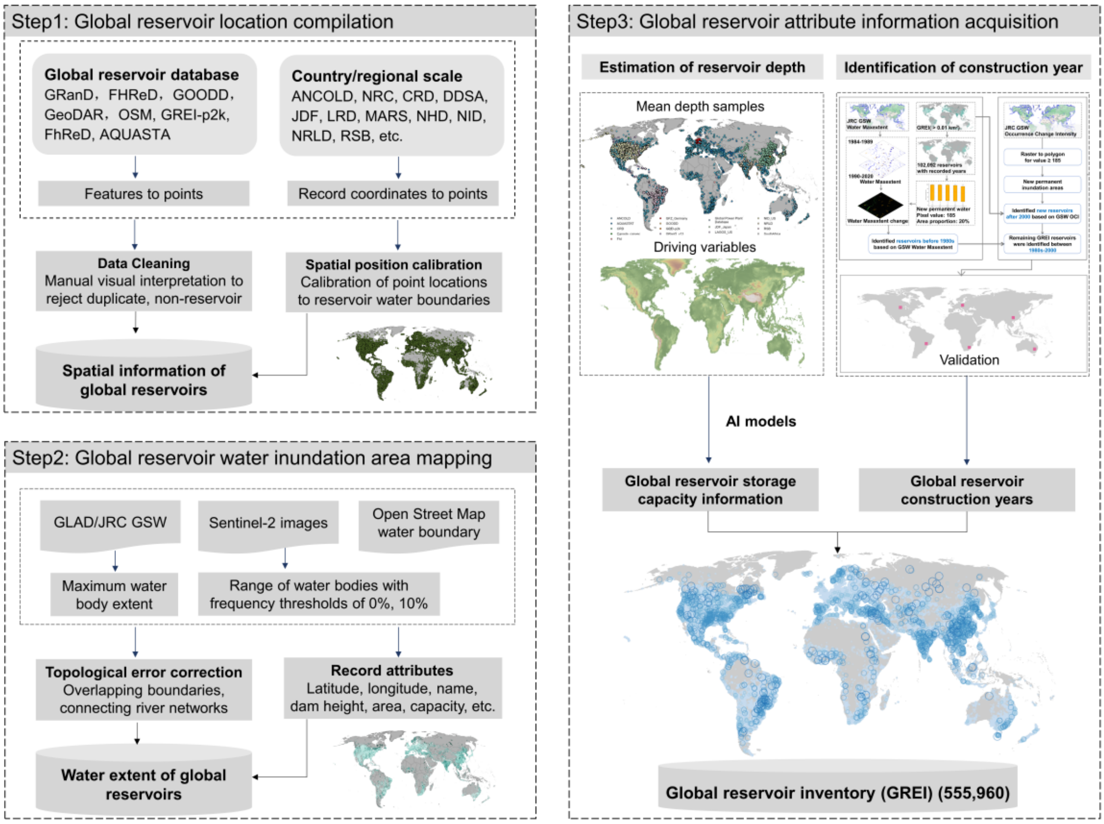

Fig. 11.

Flowchart for cataloguing the Global REservoir Inventory (GREI). This process involves three key steps: i) obtaining reservoir spatial information from multi-source datasets, ii) mapping reservoir water inundation areas based on GLAD, GSW, Sentinel-2, and other data, and iii) deriving reservoir attributes such as storage capacity and construction year using machine learning algorithms and the BFAST algorithm.

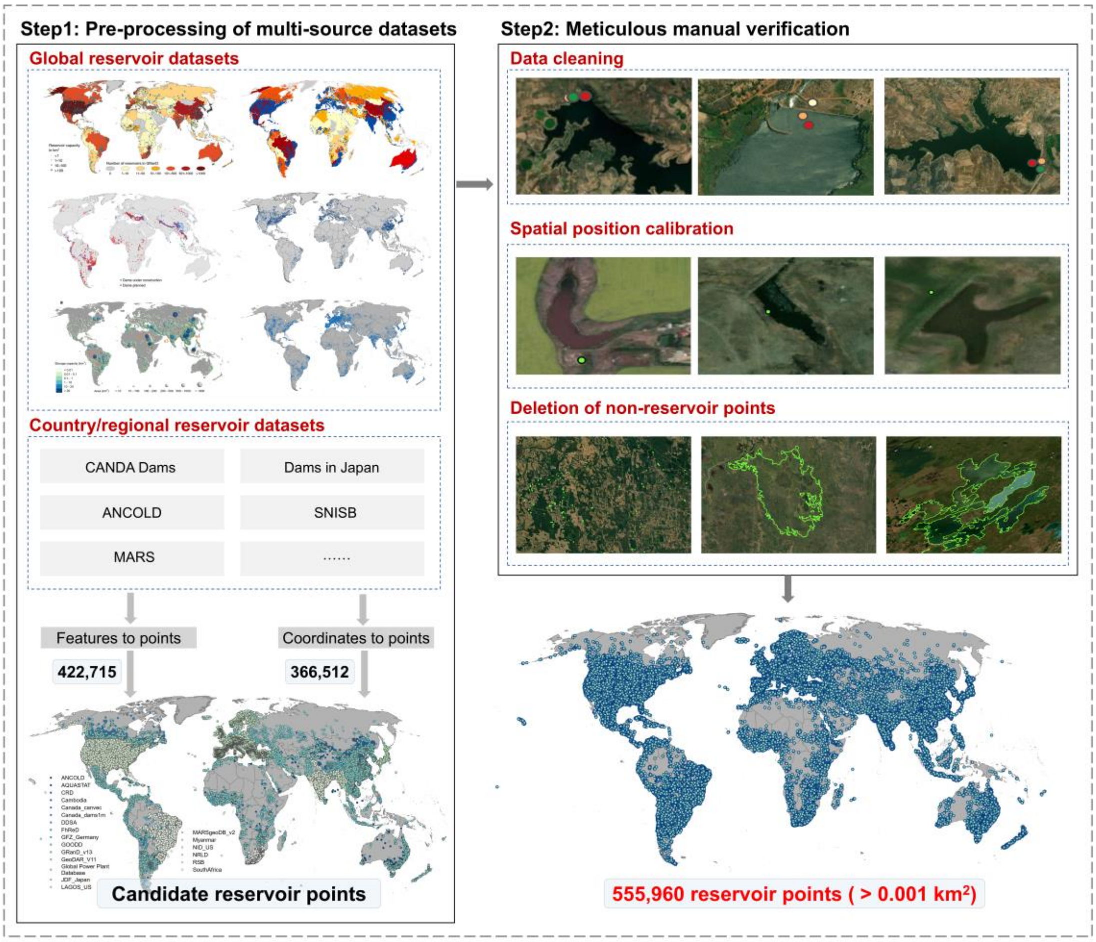

Fig. 12.

Flowchart for generating reservoir points. This process aimed primarily at systematically extracting spatial location information of reservoirs from multi-source datasets. Variations in spatial accuracy among different data sources may result in substantial geographic discrepancies for certain reservoir points and the inclusion of non-reservoir locations. To address these issues, high-resolution remote sensing imagery (e.g., ESRI World Imagery) is utilized as a geographic reference to eliminate duplicate points, perform precise spatial relocation, and remove non-reservoir points. Basemap: Esri/World Imagery. Sources: Esri, TomTom, FAO, NOAA, USGS.

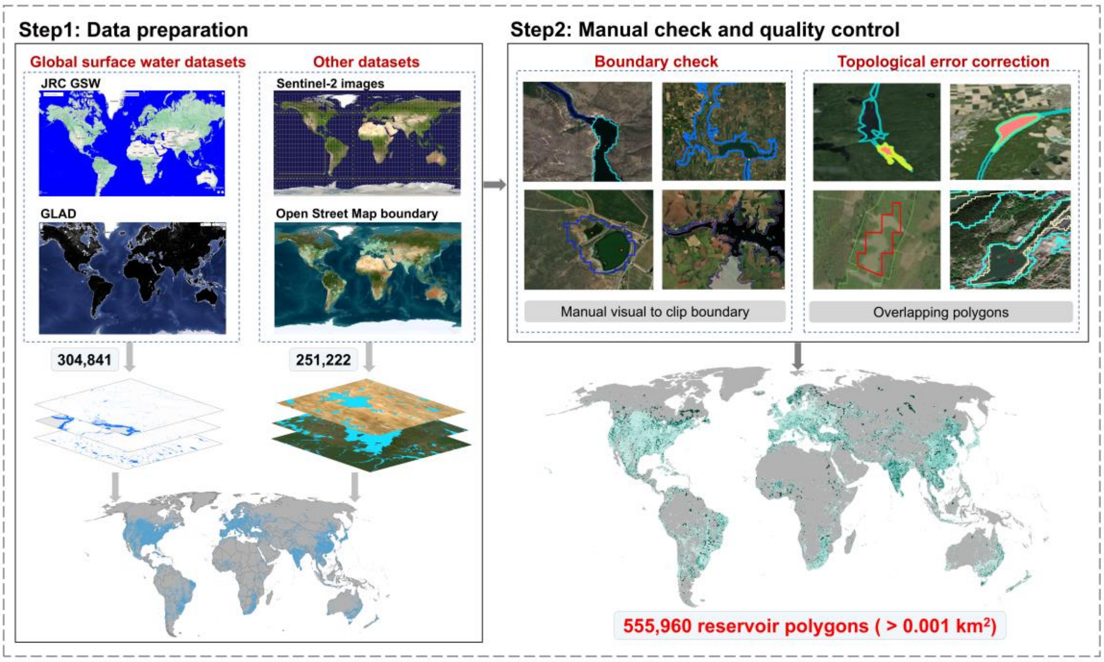

Fig. 13.

Flowchart for generating reservoir polygons. The maximum water extent of reservoirs was extracted using GSW, GLAD, and Sentinel-2 data. To address boundary complexities caused by overlaps with floodplains and alluvial areas, high-resolution imagery from ESRI World Imagery was used for manual separation and optimization. In addition, we identified topology errors such as overlaps and nested polygons, which were resolved by merging polygons for the same reservoir and correcting boundaries for different ones, ensuring improved data quality and consistency. Basemap: Esri/World Imagery. Sources: Esri, TomTom, FAO, NOAA, USGS.

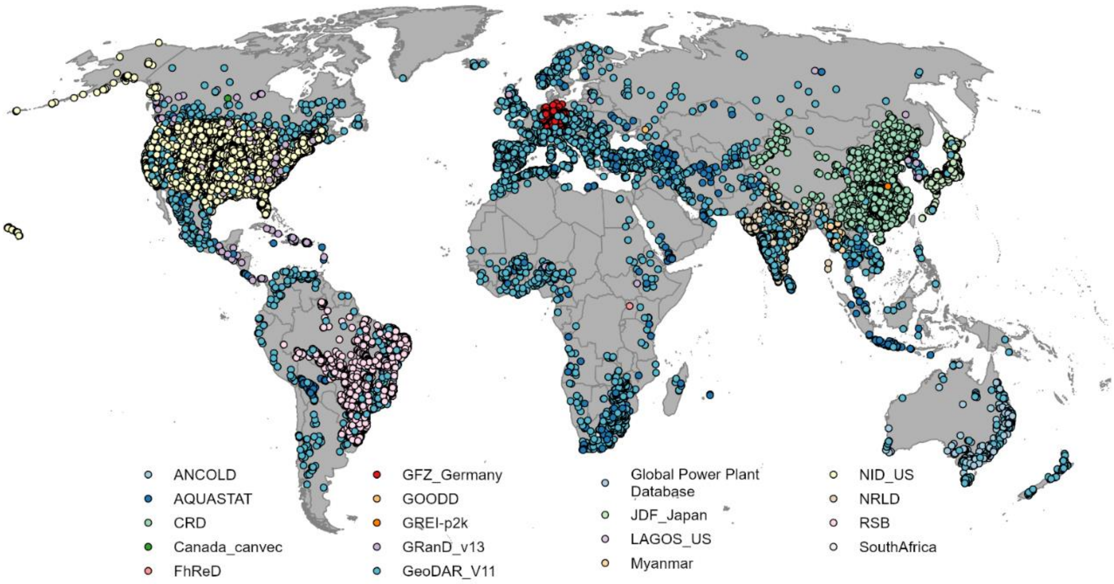

Fig. 14.

Distribution of sample data for estimating reservoir storage capacity based on the XGBoost model.

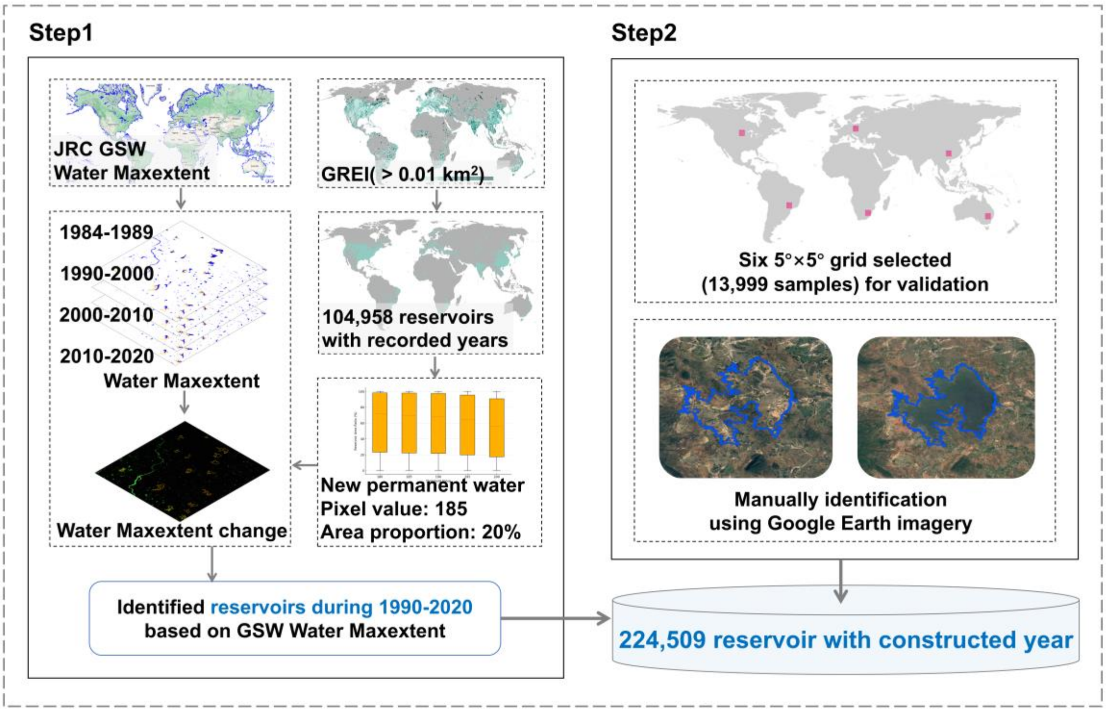

Fig. 15.

Three-step workflow for estimating the year of reservoir construction. Reservoirs larger than 0.01 km² were dated using a combination of existing records and remote sensing (GSW Water Maxextent and OCI). For smaller reservoirs, construction years were assigned based on country-level statistics. Validation was performed via manual interpretation of historical imagery. Basemap: Google Earth imagery. Source: Google.

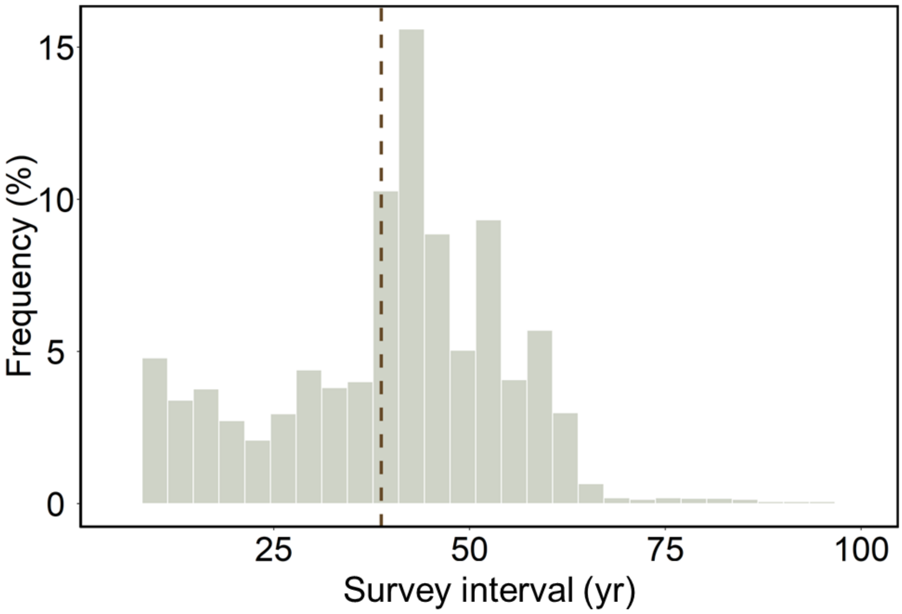

Fig. 16.

Frequency distribution of survey intervals for all selected samples. Samples with a short survey interval (<5 yr) were removed to avoid anomalous values caused by extreme weather or human activities during the two survey times.

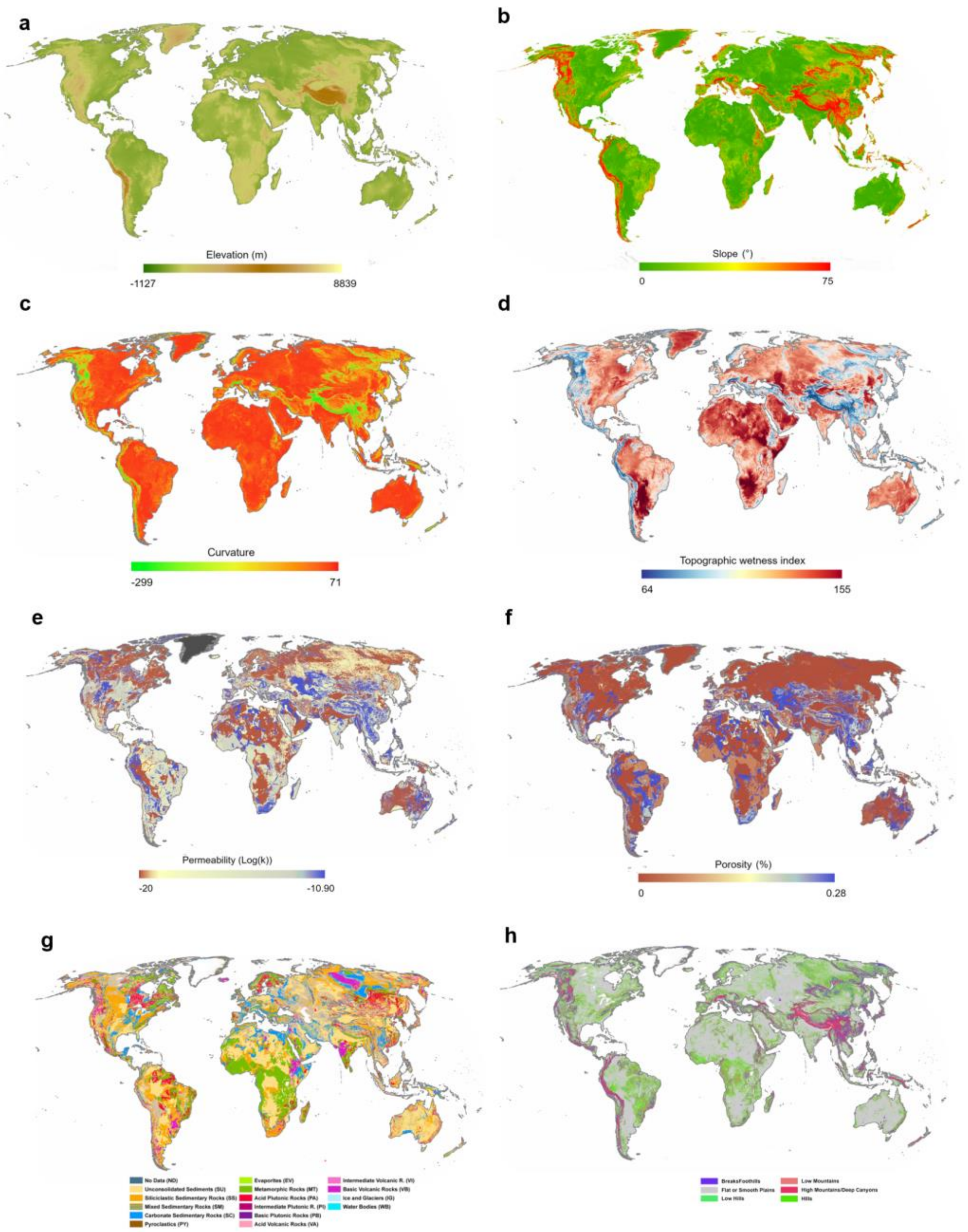

Fig. 17.

Global distribution of selected variables in geomorphology and lithology category. (a) Elevation, (b) Slope, (c) Curvature, (d) Topographic wetness index, (e) Permeability, log*(k)* is the geometric mean logarithmic permeability, (f) Porosity, (g) Lithology type, and (h) Landform type.

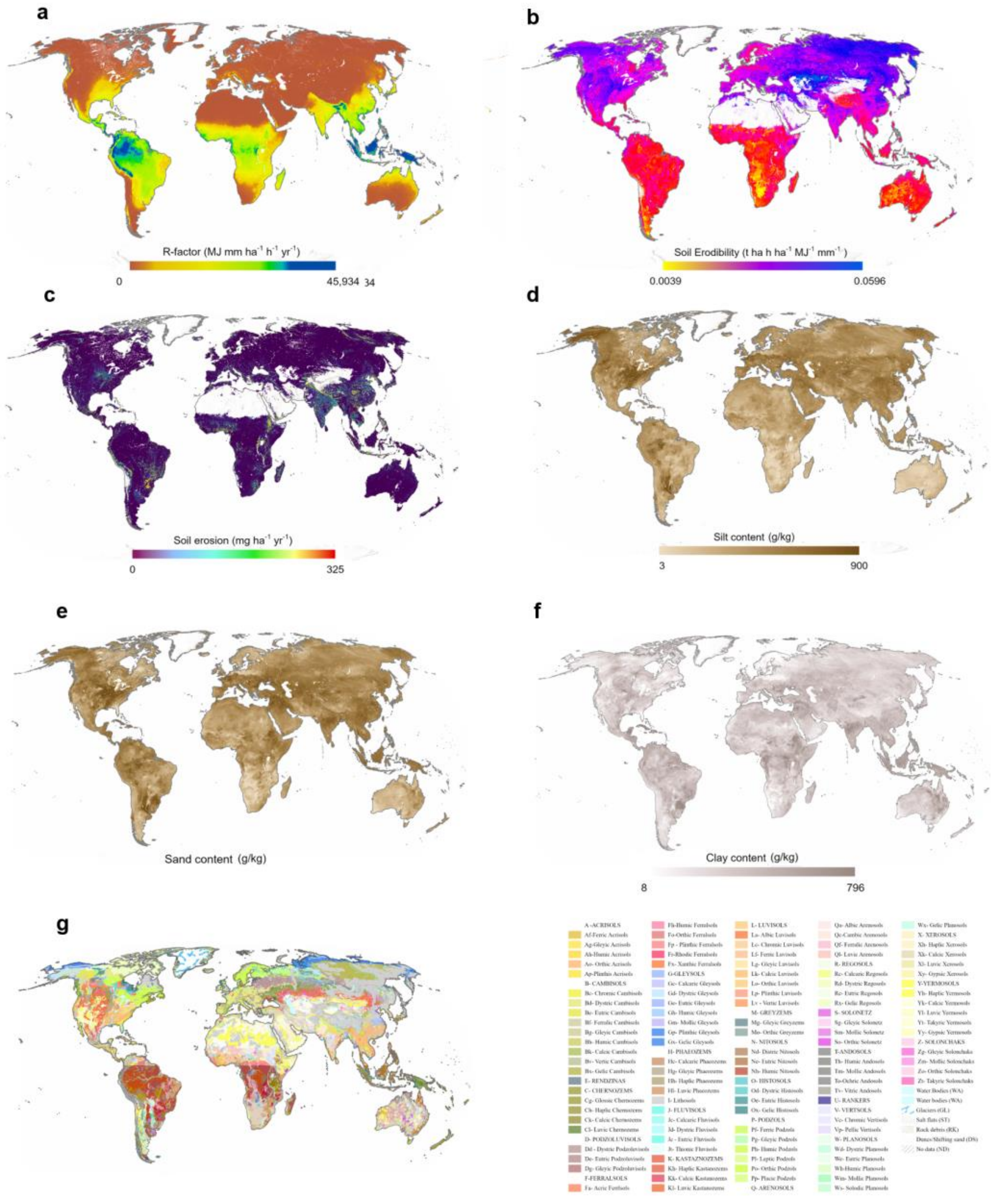

Fig. 18.

Global distribution of selected variables in soil category. (a) Rainfall Erosivity, (b) Soil Erodibility, (c) Soil Erosion, (d) Silt content, (e) Sand content, (f) Clay content, and (g) Soil type.

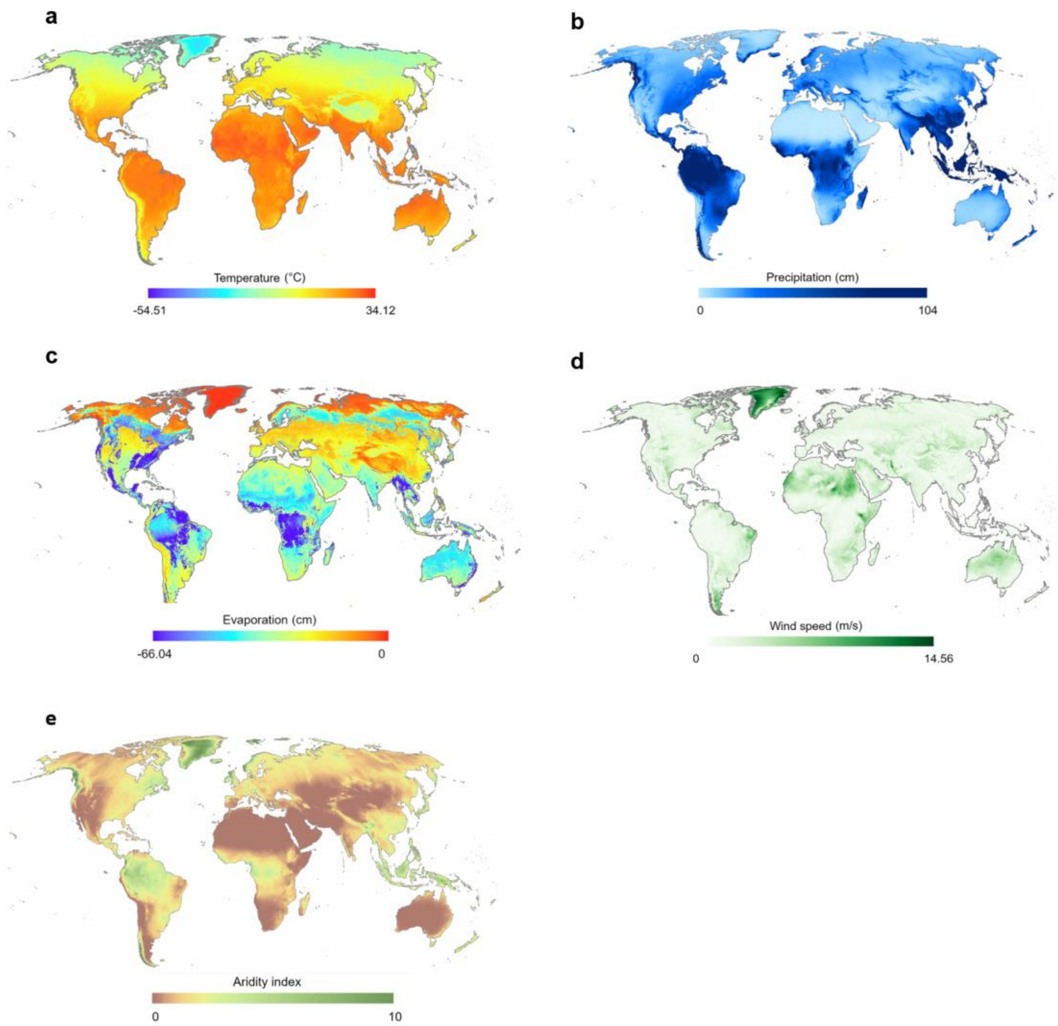

Fig. 19.

Global distribution of selected variables in climate category. (a) Temperature, (b) Precipitation, (c) Evapotranspiration, (d)Wind Speed, and (e) Aridity Index.

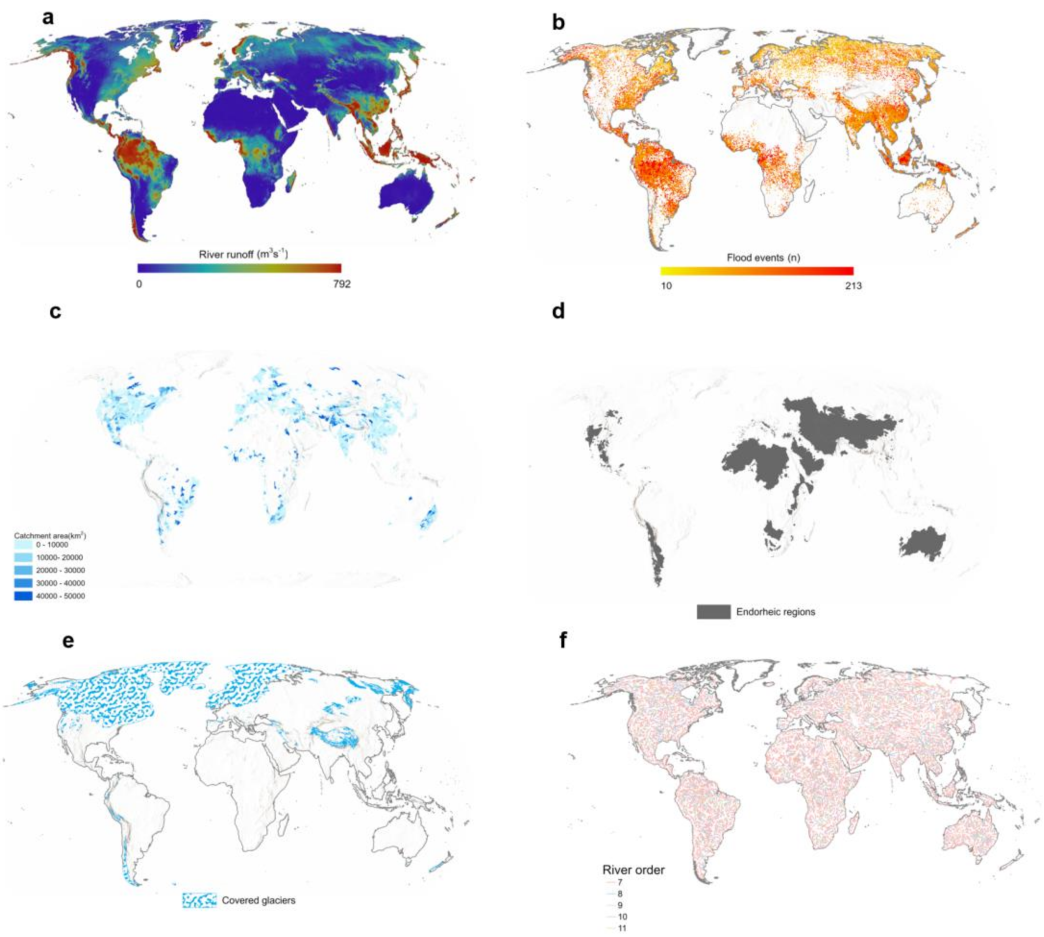

Fig. 20.

Global distribution of selected variables in hydrology category. (a) River runoff, (b) Flood events, n represents the number of flood events during 1980–2019, (c) Catchment area, (d) Endorheic basin, (e) Glacier-covered region, and (f) River order provided by HydroRIVERS.

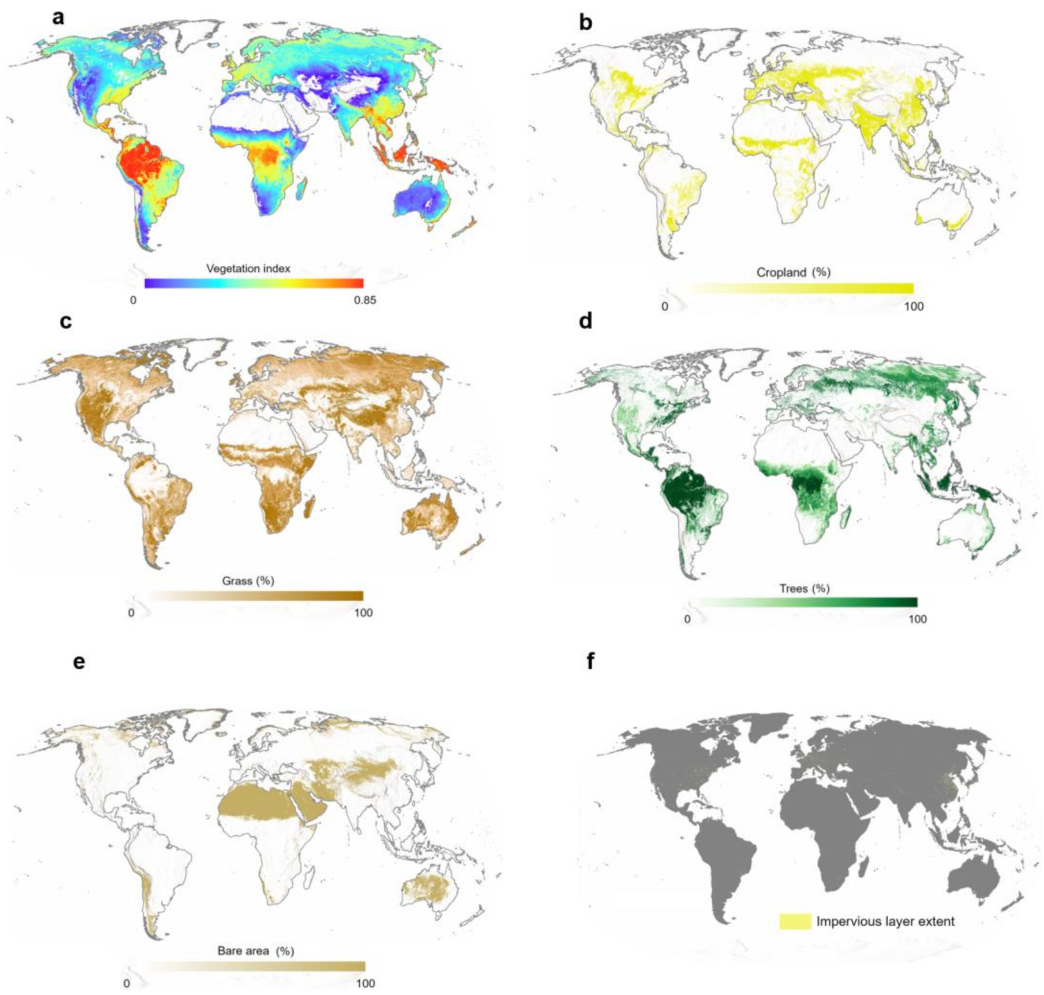

Fig. 21.

Global distribution of selected variables in land cover category. (a) Vegetation index (NDVI), (b) Cropland ratio, (c) Grass ratio, (d) Tree ratio, (e) Bare land ratio, and (f) Impervious area.

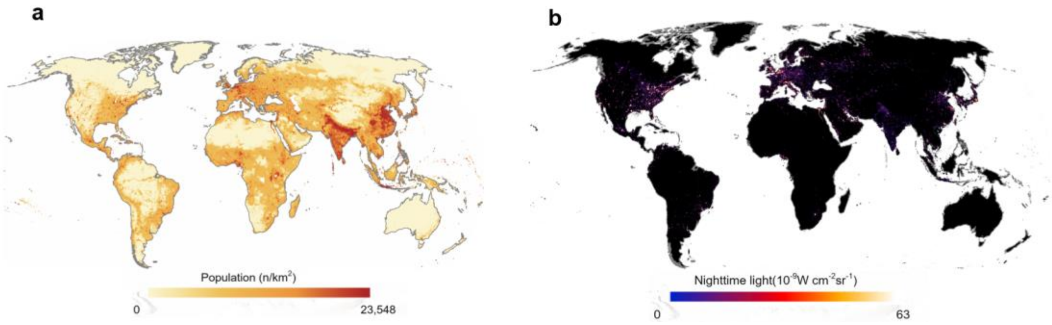

Fig. 22.

Global distribution of selected variables in human activity category. (a) Population density, (b) Nighttime light.

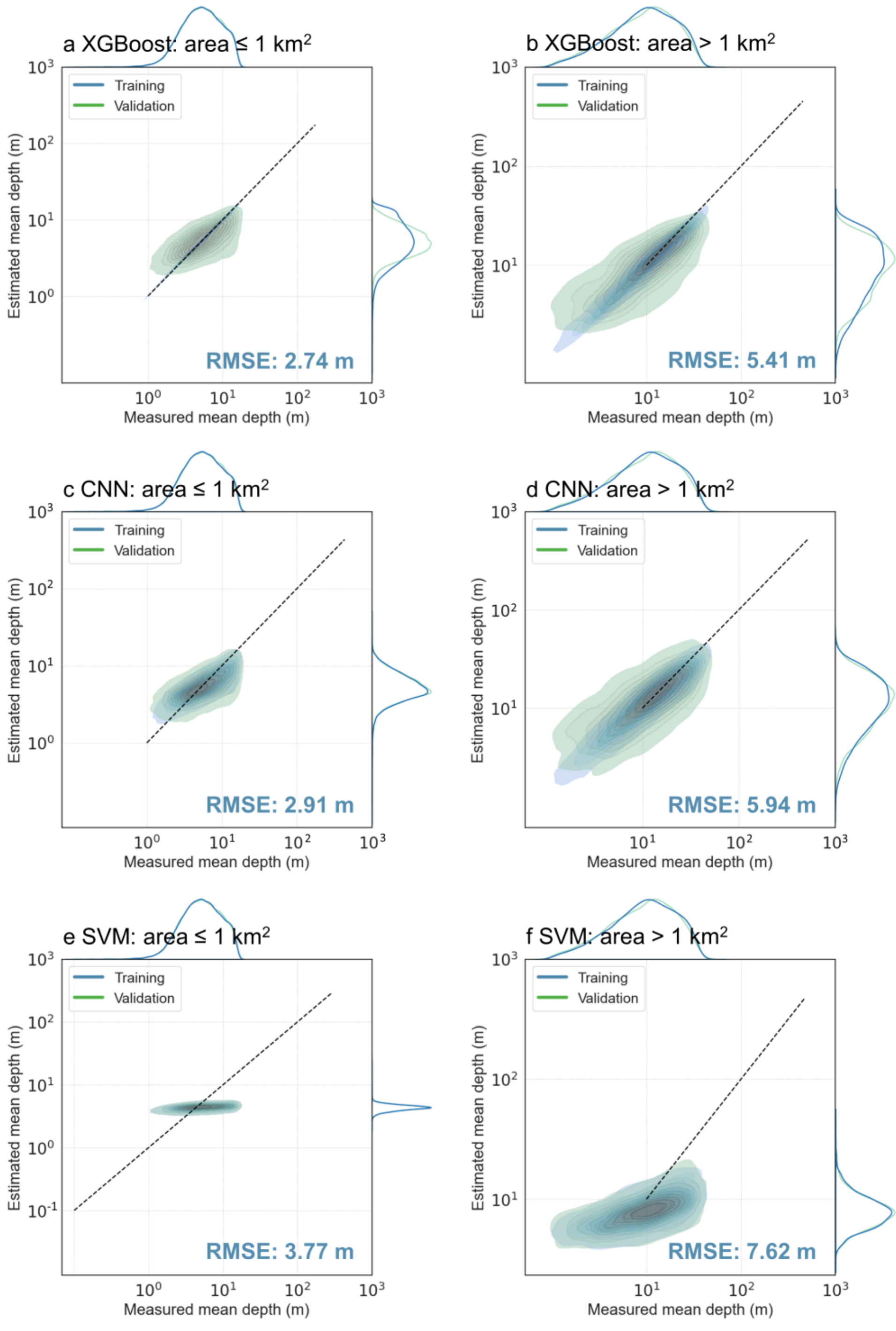

Fig. 23.

Scatter plots of training and validation sets for estimating reservoir mean depth based on the XGBoost, CNN, and SVM models, including two groups of reservoir area ≤ 1 km^2 (a, c, e) and > 1 km^2 (b, d, f).

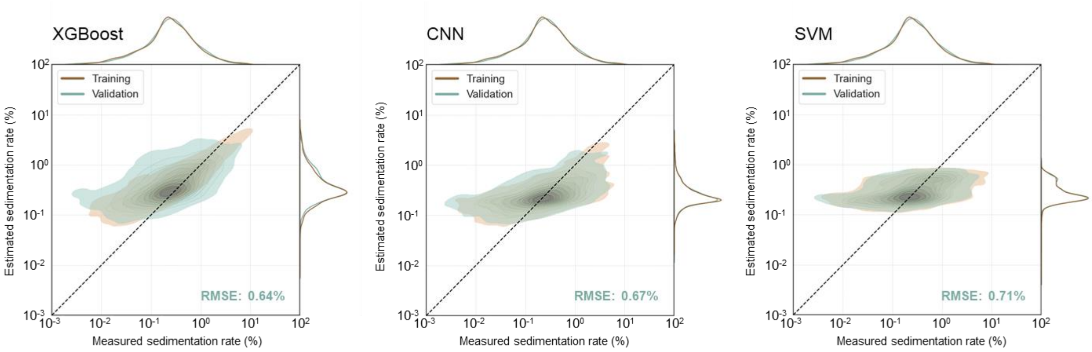

Fig. 24.

Scatter plots of training and validation sets for estimating reservoir annual sedimentation rate based on XGBoost, CNN, and SVM models.

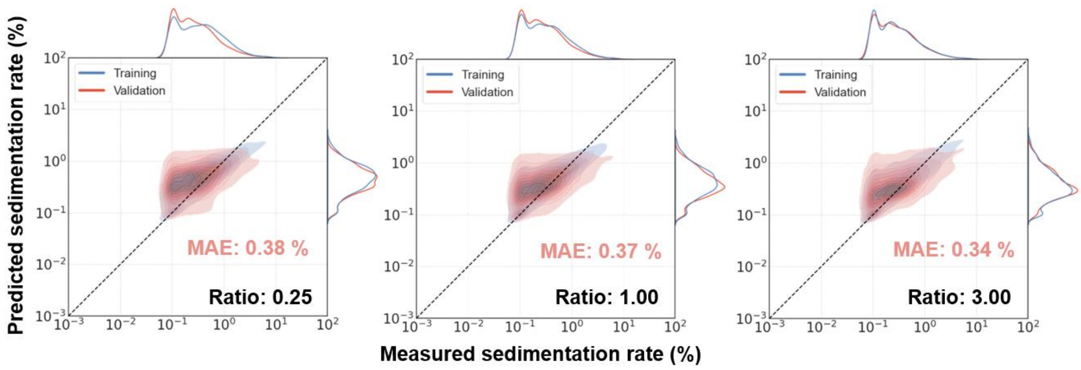

Fig. 25.

Model performance under different Chinese sample proportions. Scatter plots show predicted vs. measured sedimentation rates using Chinese-to-non-Chinese sample ratios of 0.25, 1.0, and 3.0. The model maintains stable accuracy across all sampling scenarios, demonstrating robustness to regional sample imbalance.

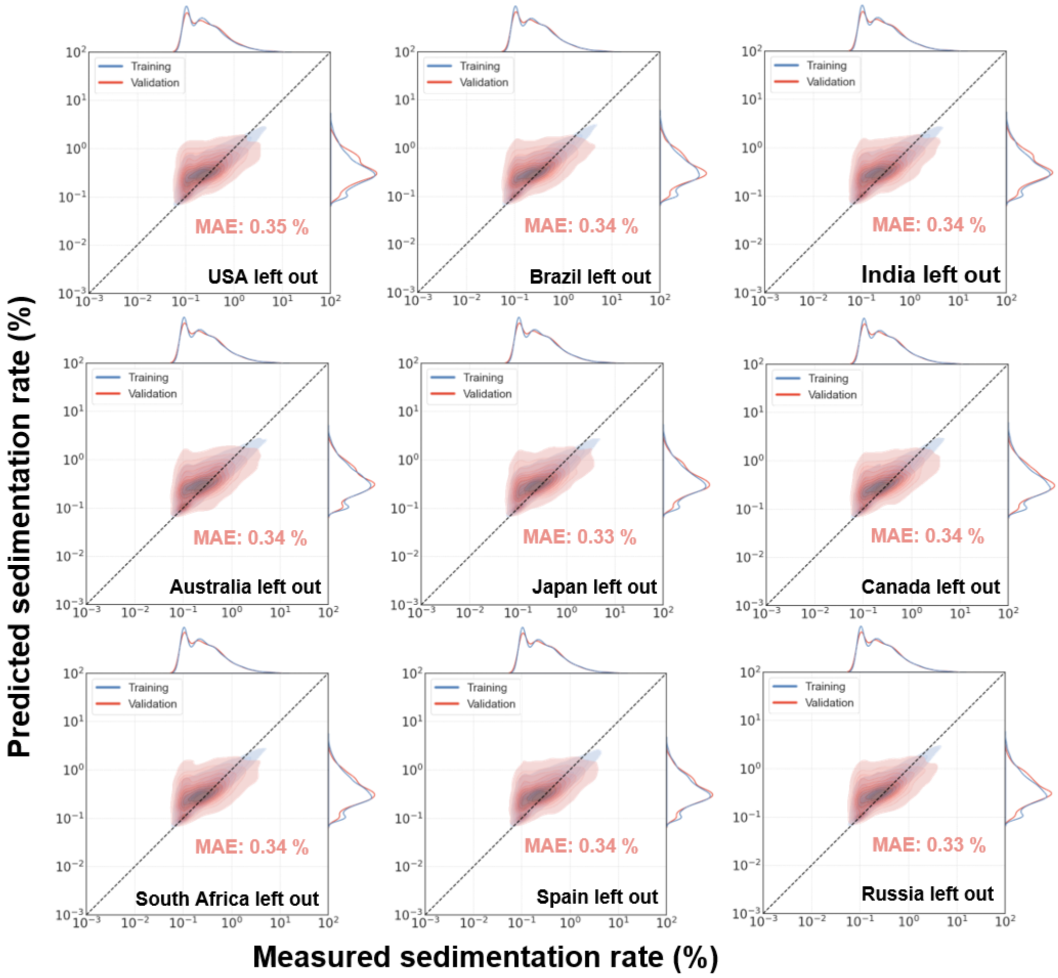

Fig. 26.

Leave-one-country-out validation of sedimentation rate predictions. Scatter plots show model performance when data from each of 10 countries are excluded during training. The low mean absolute errors (MAEs) across all cases demonstrate strong model generalizability across regions.

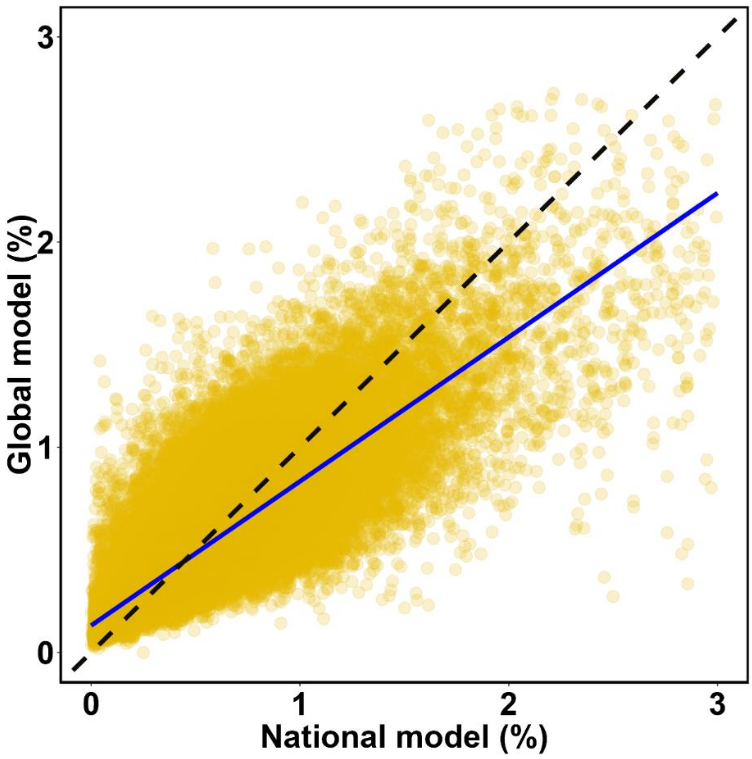

Fig. 27.

Scatter plots illustrating relationships between predictions from the national model and the global model for predicting annual sedimentation rates of reservoirs in China. The average reservoir sedimentation rates in China were estimated at 0.51% and 0.53% based on the national and global models, respectively, with an R^2 value of 0.65. This correlation indicates a high level of consistency between the results from different modeling scales. It further demonstrates that the global modeling approach employed herein can deliver accurate predictions at the national scale, making it suitable for application to individual countries.

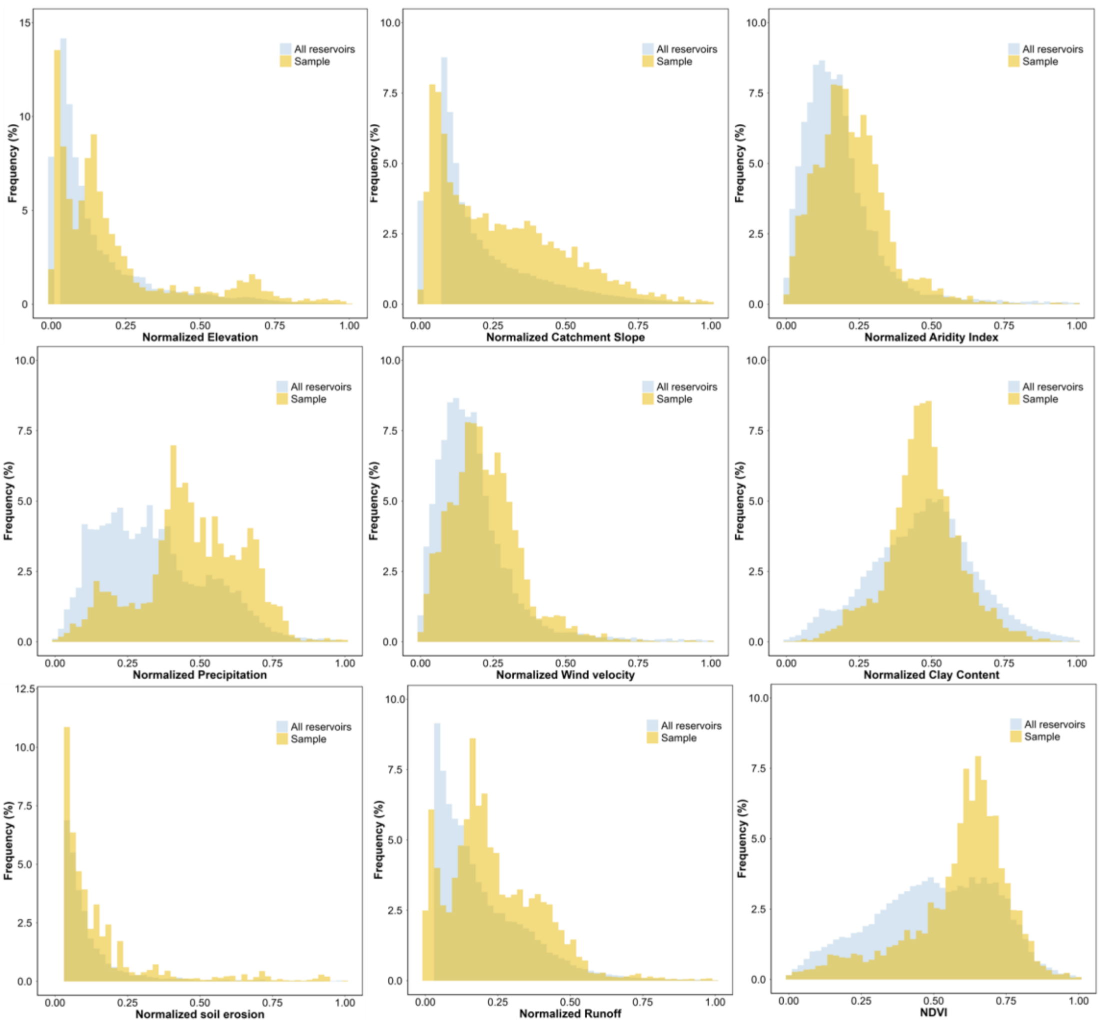

Fig. 28.

Histograms of nine selected variables representing distribution patterns between sample data and all reservoirs. The distribution patterns of the 6,133 sedimentation samples across these variables closely resemble those of the entire reservoir dataset. This similarity indicates that the sedimentation samples are representative of the overall reservoir population, facilitating the investigation of how various factors contribute to global reservoir sedimentation variability.

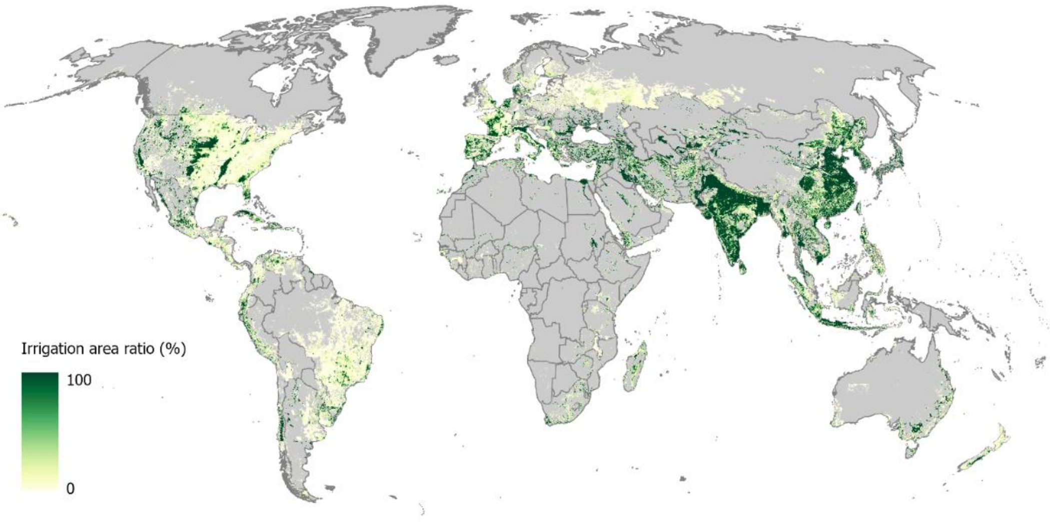

Fig. 29.

Global distribution map of irrigation areas. The map shows the areas equipped for irrigation in percentage of the total area in grid cells of 0.1° × 0.1°.

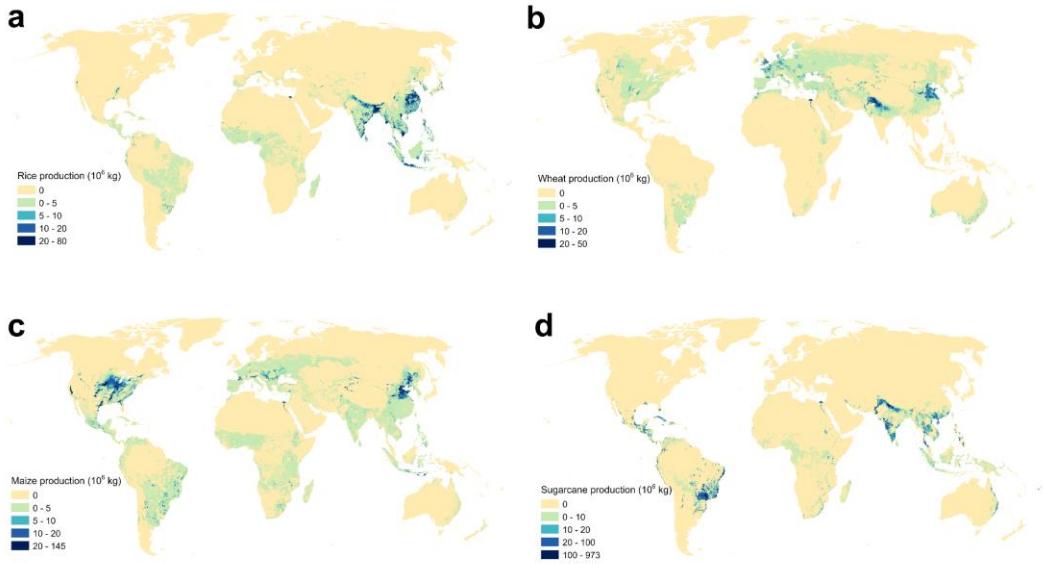

Fig. 30.

Circa 2015 annual crop production at 5-minute resolution. (a) Rice, (b) Wheat, (c) Maize, and (d) Sugarcane.

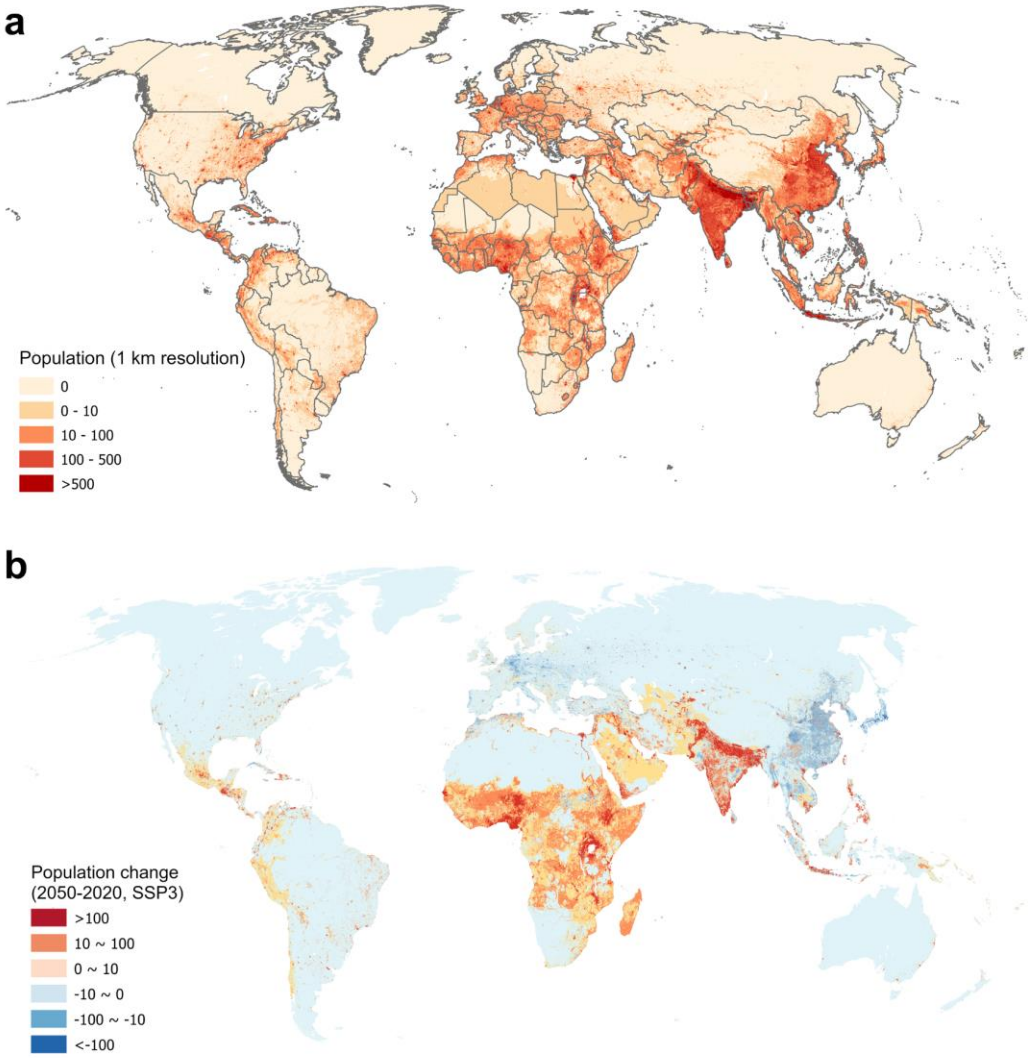

Fig. 31.

Predicted 1 km-grid global population distribution. (a) Predicted population in 2020 under the SSP3-RCP7.0 scenario, (b) Population change between 2020 and 2050 based on projected population under the SSP3–RCP7.0 scenario.

(Source: https://www.sciencedirect.com/science/article/pii/S2352340922000166)

Table 1.

Global and national regional-scale reservoir datasets referenced in the GREI data cataloguing process.

ID	Database	Region	Type	Count	Main attributes
1	**Georeferenced global dam and reservoir dataset (GeoDAR v1.1)**	**Global**	**Point and polygon**	**24,783**	**Name, area, storage, year completed, dam height, purpose**
2	**GlObal geOreferenced Database of Dams (GOODD)**	**Global**	**Point**	**32,613**	
3	**Global Reservoir and Dam (GRanD v1.3)**	**Global**	**Point and polygon**	**7,320**	**Name, area, storage**
4	**Global Reservoir Inventory of the post-2000 impoundment (GREI-p2k)**	**Global**	**Polygon**	**6,760**	**Name, area, storage, year completed**
5	**Open Street Map (OSM)**	**Global**	**Polygon**	**773,261**	**Name, area**
6	**AQUASTAT – FAO's Global Information System on Water and Agriculture**	**Global**	**Point**	**10,808**	**Area, storage, year completed, dam height, etc.**
7	**Global Power Plant Database (FHReD)**	**Global**	**Point**	**3,700**	**Name, year completed**
8	Australian National Committee on Large Dams (ANCOLD)	Australia	Point	739	Storage
9	CanVec (NRC, 2017)	Canada	Point, line and polygon	46,104	
10	China Reservoir Dataset (CRD)	China	Polygon	97,435	Name, area, storage,
11	Dataset of Georeferenced Dams in South America (DDSA) v1.0.2	South America	Point	1,010	Name, purposes and georeferenced location
12	Inventory of dams in Germany	Germany	Point	530	Name, area, storage, year completed, dam height, purpose
13	Japan Dam Foundation (JDF)	Japan	Point	2,421	Area, storage, year completed, dam height, etc.
14	LAGOS-US RESERVOIR v1	United states	Point and polygon	61,042	Area
15	List of Registered Dams LRD (DWS, 2019)	South Africa	Point	5,636	Area, storage
16	Inventory of Large Dams in Canada 2019	Canada	Point	1,157	Surface area, storage, year completed, dam height, etc.
17	Managing Aquatic ecosystems and water Resources under multiple Stress project (MARS) (2017)	Europe	Point	5,043	Name, area, storage, year completed, dam height, etc.
18	National Hydrography Dataset (NHD)	United states	Point and polygon	360,567	Area
19	National Inventory of Dams (NID) (USACE, 2013)	United states	Point and polygon	96,071	Surface Area, NID Storage, year completed, dam height, etc.

20	National Register of Large Dams (NRLD) in India	India	Point	5,701	Area, storage, year completed, dam height, etc.
21	Open Development Cambodia (ODC) (2015)	Cambodia	Point	73	Storage, year completed, dam height, purpose
22	Open Development Myanmar (ODM) (2018)	Myanmar	Point	254	Storage, year completed, dam height
23	Relatório de Segurança de Barragens (RSB) (SNISB, 2017)	Brazil	Point	24,097	Storage, dam height

Table 2.

Statistics on the reservoir capacity and sedimentation rate in different continents.

Continent	Reservoir number	Annual sedimentation rate (%)	Annual total sediments (10^8 m^3)	Reservoir storage capacity (10^8 m^3)	Annual capacity loss rate (%)
Africa	24,738	0.78	42.32	9,794.68	0.43
Asia	185,167	0.63	140.42	29,880.59	0.47
Europe	82,960	0.70	26.40	6,443.10	0.41
North America	184,286	0.78	90.16	18,227.75	0.49
Oceania	24,399	0.99	6.51	1,021.28	0.64
South America	54,410	0.81	55.35	10,405.44	0.53
World	555,960	0.73	361.16	75,772.85	0.48

Table 3.

Statistics on reservoir capacity and sedimentation rate in different countries (countries with fewer than 50 reservoirs excluded).

Country	Reservoir number	Annual sedimentation rate (%)	Annual total sediments (10^8 m^3)	Reservoir storage capacity (10^8 m^3)	Annual capacity loss rate (%)
Afghanistan	98	0.96	0.41	53.84	0.77
Albania	422	0.46	0.24	51.41	0.46
Algeria	367	0.86	0.66	94.26	0.70
Angola	127	0.83	1.18	203.06	0.58
Argentina	3,886	0.98	3.67	832.32	0.44
Armenia	261	0.69	0.05	11.04	0.44
Australia	22,821	0.99	6.12	950.96	0.64
Austria	638	0.46	0.09	33.36	0.26
Azerbaijan	131	0.72	1.55	220.96	0.70
Bangladesh	1,934	0.83	0.22	66.63	0.34
Belarus	1,120	0.59	0.13	32.83	0.39
Belgium	255	0.58	0.01	2.84	0.45
Benin	66	0.76	0.00	0.52	0.54
Bolivia	2,188	0.83	0.21	33.85	0.63
Bosnia and Herzegovina	134	0.63	0.12	40.59	0.29
Botswana	96	1.20	0.09	11.52	0.78
Brazil	39,623	0.77	33.07	6,363.89	0.52
Bulgaria	1,273	0.84	0.40	77.32	0.52
Burkina Faso	455	0.80	0.36	67.81	0.53
Cambodia	156	0.81	0.31	48.99	0.64
Canada	17,226	0.72	33.80	7,271.47	0.46
Canarias	365	0.94	0.00	0.51	0.81
Chile	3,047	0.84	0.82	190.31	0.43
China	107,791	0.54	45.02	10,292.10	0.44
Colombia	1,418	1.02	1.83	235.72	0.78
Congo, Democratic	106	0.96	0.35	56.63	0.61
Costa Rica	124	1.13	0.16	25.90	0.61
Cote D'Ivoire	157	0.59	1.58	384.29	0.41
Croatia	114	0.74	0.08	14.73	0.54
Cuba	2,041	0.97	0.58	83.74	0.70
Cyprus	173	0.84	0.02	3.39	0.62
Czech Republic	6,209	0.60	0.11	41.45	0.28
Denmark	105	0.46	0.00	1.25	0.26
Dominican Republic	53	0.94	0.22	32.06	0.69
Egypt	209	0.71	1.49	1,658.55	0.09
Eritrea	138	1.12	0.04	4.88	0.90
Estonia	242	0.57	0.00	0.79	0.48
Ethiopia	206	0.96	7.84	1,070.98	0.73
Finland	582	0.61	0.37	90.97	0.40
France	6,682	0.62	0.61	138.22	0.44
Georgia	268	0.64	0.19	35.52	0.53
Germany	2,699	0.52	0.22	68.21	0.32
Ghana	161	0.73	7.45	1,611.91	0.46
Greece	576	0.71	0.54	137.96	0.39
Guatemala	93	1.17	0.04	4.97	0.71
Honduras	62	1.05	0.60	71.86	0.83
Hungary	475	0.75	0.03	5.06	0.64
Iceland	59	0.67	0.24	53.55	0.45
India	28,719	0.80	24.49	4,127.11	0.59
Indonesia	1,177	1.03	1.92	221.72	0.86
Iran	1,313	0.90	5.40	591.96	0.91
Iraq	392	0.97	2.39	665.46	0.36
Ireland	57	0.50	0.01	3.82	0.33
Italy	6,530	0.85	0.68	139.28	0.49

Japan	20,463	0.69	1.50	256.62	0.59
Jordan	167	1.01	0.02	2.53	0.75
Kazakhstan	836	0.57	2.57	597.66	0.43
Kenya	475	0.94	0.23	42.73	0.54
Korea, South	340	0.39	0.46	205.56	0.22
Korea, North	168	0.33	0.97	290.86	0.33
Kyrgyzstan	183	0.80	1.41	241.34	0.58
Laos	880	0.75	2.12	291.42	0.73
Latvia	618	0.50	0.09	11.13	0.83
Lesotho	68	0.57	0.05	29.78	0.17
Lithuania	3,869	0.46	0.07	21.76	0.32
Macedonia, Republic	65	0.54	0.05	24.94	0.21
Madagascar	66	0.64	0.03	8.42	0.39
Malawi	57	0.86	0.00	0.60	0.75
Malaysia	248	0.92	3.52	835.07	0.42
Mali	83	0.84	0.49	139.25	0.35
Mexico	7,678	1.02	6.40	1,270.49	0.50
Moldova	772	0.99	0.31	34.22	0.90
Morocco	362	0.84	0.88	186.94	0.47
Mozambique	73	0.65	2.43	691.25	0.35
Myanmar	716	0.84	1.83	291.02	0.63
Namibia	604	1.83	0.20	14.19	1.44
Nepal	3,791	0.94	0.13	14.92	0.87
Netherlands	242	0.60	0.01	1.65	0.53
New Zealand	1,343	0.90	0.36	65.52	0.55
Nigeria	415	0.79	2.58	389.81	0.66
Norway	816	0.66	2.59	507.92	0.51
Pakistan	588	1.08	3.66	350.07	1.05
Panama	192	1.05	0.30	59.32	0.50
Paraguay	2,367	0.90	2.61	425.97	0.61
Peru	693	0.97	0.46	73.12	0.63
Philippines	332	1.14	0.89	99.35	0.90
Poland	6,534	0.59	0.15	47.76	0.31
Portugal	8,440	1.00	1.18	185.81	0.63
Puerto Rico	84	1.07	0.04	4.94	0.77
Romania	701	0.93	0.51	95.79	0.54
Russian Federation	9,771	0.56	28.30	8,599.25	0.33
Saudi Arabia	176	0.83	0.14	14.25	1.00
Senegal	89	0.89	0.05	5.70	0.83
Serbia	209	0.68	0.28	57.95	0.48
Slovakia	366	0.64	0.06	20.59	0.29
Slovenia	74	0.48	0.02	3.74	0.41
Somalia	423	0.99	0.00	0.34	0.90
South Africa	15,497	0.72	1.26	385.67	0.33
South Sudan	65	0.74	0.00	0.61	0.61
Spain	11,334	0.84	2.69	608.67	0.44
Sri Lanka	2,405	0.82	0.50	101.77	0.49
Sudan	116	0.86	1.11	136.67	0.81
Swaziland	72	0.65	0.02	7.21	0.27
Sweden	872	0.60	1.03	248.41	0.41
Switzerland	304	0.59	0.16	60.37	0.26
Syrian Arab Republic	444	0.88	0.81	159.89	0.50
Tajikistan	68	0.92	2.69	297.54	0.90
Tanzania	161	0.89	0.31	49.96	0.62
Thailand	6,092	0.65	4.93	854.75	0.58
Tunisia	434	0.91	0.22	31.21	0.69
Turkey	2,481	0.65	8.10	1,988.15	0.41
Turkmenistan	84	0.76	0.84	142.03	0.59
Ukraine	6,573	0.73	2.01	555.52	0.36
United Arab Emirates	126	0.98	0.01	1.10	0.77
United Kingdom	2,883	0.47	0.27	84.47	0.32
United States	156,809	0.77	47.84	9,378.30	0.51
Uruguay	699	0.62	1.31	224.05	0.58

Uzbekistan	637	0.77	1.00	184.44	0.54
Venezuela	421	0.81	9.19	1,633.83	0.56
Viet Nam	1,480	0.76	2.72	612.36	0.44
Yemen	147	1.13	0.06	4.34	1.41
Zambia	865	0.86	0.91	148.97	0.61
Zimbabwe	1,996	0.73	8.45	1,958.66	0.43

Table 4.

Statistics on the reservoir capacity and sedimentation rate in different basins (basins with fewer than 50 reservoirs excluded).

Basin	Reservoir number	Annual sedimentation rate (%)	Annual total sediments (10^8 m^3)	Reservoir storage capacity (10^8 m^3)	Annual capacity loss rate (%)
Adriatic Sea - Greece - Black Sea Coast	2,389	0.70	1.41	335.11	0.42
Africa, East Central Coast	275	0.88	0.43	73.87	0.58
Africa, Indian Ocean Coast	410	0.63	0.26	73.50	0.35
Africa, North Interior	143	0.76	0.10	17.34	0.56
Africa, North West Coast	640	0.91	0.70	168.57	0.42
Africa, Red Sea - Gulf of Aden Coast	300	1.05	0.04	3.98	0.92
Africa, South Interior	116	1.33	0.04	4.56	0.93
Africa, West Coast	334	0.72	2.37	515.66	0.46
Amazon	3,840	0.79	2.13	455.08	0.47
Amu Darya	259	0.83	3.12	410.40	0.76
Amur	3,484	0.60	6.01	1,513.71	0.40
Angola, Coast	105	0.79	1.17	201.54	0.58
Arabian Peninsula	296	0.89	0.09	9.04	0.97
Arabian Sea Coast	219	0.90	0.61	30.99	1.98
Atlantic Ocean Seaboard	6,287	0.57	2.40	570.74	0.42
Australia, East Coast	5,379	0.88	1.66	264.47	0.63
Australia, Interior	1,120	0.86	0.04	5.38	0.76
Australia, North Coast	350	0.89	0.77	122.06	0.63
Australia, South Coast	1,561	1.09	0.03	3.67	0.70
Australia, West Coast	4,258	1.23	0.13	16.96	0.79
Baja California	57	1.13	0.02	4.58	0.53
Baltic Sea Coast	1,643	0.51	0.05	10.61	0.47
Bay of Bengal, North East Coast	394	1.01	0.22	65.73	0.33
Black Sea, North Coast	2,461	0.79	0.40	74.95	0.54
Black Sea, South Coast	1,152	0.60	1.87	410.01	0.46
Bo Hai - Korean Bay, North Coast	1,777	0.70	2.33	604.94	0.38
Brahmani	200	0.68	0.48	74.56	0.64
California	4,879	0.99	3.79	550.80	0.69
Caribbean	2,260	0.98	0.87	124.14	0.70
Caribbean Coast	466	0.90	0.56	90.91	0.61
Caspian Sea Coast	298	0.68	0.30	53.42	0.56
Caspian Sea, East Coast	261	0.81	0.92	102.55	0.89
Caspian Sea, South West Coast	787	0.72	2.94	365.87	0.80
Cauvery	1,005	0.77	0.52	116.81	0.45
Central Iran	424	0.93	0.45	58.78	0.77
Chao Phraya	861	0.78	1.81	325.84	0.55
China Coast	22,974	0.59	4.00	1,502.61	0.27
Columbia and Northwestern United States	4,271	0.86	7.40	1,185.41	0.62
Congo	176	0.91	0.44	72.04	0.61
Danube	5,380	0.72	1.29	287.14	0.45
Daugava	353	0.45	0.09	13.63	0.69
Dead Sea	199	0.95	0.05	6.15	0.84
Denmark - Germany Coast	264	0.53	0.00	1.37	0.28
Dnieper	4,013	0.66	1.59	491.23	0.32
Dniester	846	0.89	0.50	68.87	0.73
Don	5,600	0.56	0.90	299.37	0.30

Douro	476	0.72	0.51	104.79	0.49
East Brazil, South Atlantic Coast	12,822	0.75	1.85	270.53	0.68
Eastern Jordan - Syria	142	0.94	0.01	1.40	0.88
Ebro	2,058	0.77	0.28	86.56	0.32
Elbe	4,825	0.55	0.12	52.96	0.23
Ems - Weser	572	0.53	0.03	7.19	0.41
England and Wales	2,334	0.46	0.08	27.89	0.30
Finland	529	0.61	0.36	90.40	0.40
France, South Coast	237	0.72	0.04	7.47	0.49
France, West Coast	1,636	0.60	0.03	6.87	0.43
Fraser	285	0.71	0.85	283.31	0.30
Ganges - Brahmaputra	10,713	0.87	8.60	1,159.87	0.74
Gironde	2,055	0.57	0.15	36.86	0.40
Gobi Interior	1,044	0.81	0.61	82.49	0.74
Godavari	4,035	0.77	3.21	543.32	0.59
Great Basin	1,334	0.99	0.48	72.04	0.66
Grijalva - Usumacinta	346	0.89	1.06	227.67	0.47
Guadalquivir	920	0.91	0.41	84.96	0.48
Guadiana	4,031	0.97	1.20	197.29	0.61
Gulf Coast	13,234	0.84	5.20	822.86	0.63
Gulf of Guinea	54	0.86	0.77	164.57	0.47
Gulf of Mexico, North Atlantic Coast	31,887	0.69	4.71	824.92	0.57
Gulf of Thailand Coast	371	0.82	0.27	40.49	0.67
Hainan	1,026	0.70	0.47	114.29	0.41
Helmand	83	0.94	0.20	35.86	0.56
Hong (Red River)	1,547	0.81	1.18	346.28	0.34
Huang He	4,712	0.92	7.99	919.55	0.87
Hudson Bay Coast	146	0.53	12.28	2,260.67	0.54
Iceland	59	0.67	0.24	53.55	0.45
India East Coast	1,079	0.73	0.20	47.73	0.43
India North East Coast	143	0.72	0.11	22.05	0.51
India South Coast	2,109	0.77	0.36	88.51	0.41
India West Coast	967	0.91	1.00	219.25	0.46
Indus	751	1.07	4.60	599.10	0.77
Ireland	127	0.51	0.02	6.18	0.33
Irrawaddy	663	0.83	1.03	184.03	0.56
Isthmus of Tehuantepec	83	0.91	0.06	11.94	0.51
Italy, East Coast	2,117	0.83	0.17	33.54	0.51
Italy, West Coast	816	0.72	0.10	16.48	0.60
Japan	20,446	0.69	1.50	256.41	0.59
Java - Timor	631	0.97	0.85	115.05	0.74
Kalimantan	177	1.12	0.15	20.39	0.76
Krishna	4,041	0.78	3.83	679.43	0.56
La Plata	18,830	0.81	21.66	3,980.31	0.54
La Puna Region	223	1.08	0.23	28.50	0.82
Lake Balkhash	294	0.75	1.53	340.33	0.45
Lake Chad	82	0.79	0.21	38.33	0.55
Limpopo	1,758	0.75	0.37	86.33	0.43
Loire	943	0.70	0.06	11.28	0.56
Maas	208	0.56	0.02	6.52	0.34
Mackenzie	168	0.66	3.64	780.47	0.47
Madagascar	84	0.67	0.04	9.38	0.42
Magdalena	952	1.06	1.49	179.33	0.83
Mahanadi	2,285	0.73	1.02	207.46	0.49

Mahi	1,265	0.89	0.56	74.41	0.75
Mar Chiquita	152	0.83	0.16	30.76	0.52
Mediterranean Sea Islands	2,379	0.99	0.20	36.61	0.55
Mediterranean Sea, East Coast	1,025	0.68	1.79	337.58	0.53
Mediterranean South Coast	849	0.88	1.03	136.76	0.76
Mekong	6,186	0.62	4.81	993.61	0.48
Mexico, Interior	850	1.10	0.15	42.93	0.35
Mexico, Northwest Coast	3,109	1.07	1.45	298.01	0.49
Mississippi - Missouri	73,987	0.80	20.28	4,262.91	0.48
Murray - Darling	9,338	0.95	1.66	315.04	0.53
Namibia, Coast	279	1.94	0.03	2.39	1.33
Narmada	936	0.76	1.31	230.71	0.57
Narva	137	0.61	0.00	0.34	0.59
Negro	86	0.92	1.56	437.89	0.36
Neman	3,175	0.46	0.12	33.00	0.36
Neva	248	0.52	0.04	10.66	0.41
New Zealand	1,343	0.90	0.36	65.52	0.55
Niger	562	0.78	2.81	455.25	0.62
Nile	650	0.92	9.23	2,660.72	0.35
North America, Colorado	5,323	1.06	2.67	930.30	0.29
North and South Korea	479	0.37	0.90	361.95	0.25
North Argentina, South Atlantic Coast	201	0.80	0.29	50.90	0.56
North Borneo Coast	54	1.04	2.25	587.14	0.38
North Brazil, South Atlantic Coast	314	0.84	0.08	15.54	0.54
North Chile, Pacific Coast	1,478	0.89	0.16	29.31	0.54
North Gulf	125	0.83	0.25	48.09	0.53
Northwest Territories	64	0.64	1.02	241.89	0.42
Ob	474	0.53	1.49	259.32	0.58
Oder	3,169	0.61	0.06	20.32	0.28
Orange	3,794	0.83	0.88	245.76	0.36
Orinoco	390	0.83	8.94	1,593.69	0.56
Pacific and Arctic Coast	958	0.79	1.23	187.41	0.65
Pacific Central Coast	79	1.00	0.10	16.31	0.61
Pampas Region	262	0.88	0.17	27.32	0.61
Parnaiba	467	0.71	0.40	68.53	0.58
Peninsula Malaysia	785	0.90	3.49	612.95	0.57
Pennar	920	0.75	0.37	67.01	0.56
Persian Gulf Coast	79	0.90	0.41	52.77	0.78
Peru, Pacific Coast	411	1.05	0.27	39.27	0.68
Philippines	332	1.14	0.89	99.35	0.90
Po	821	0.68	0.17	48.62	0.35
Poland Coast	613	0.49	0.01	1.39	0.43
Red Sea, East Coast	178	1.11	0.15	13.30	1.12
Rhine	1,329	0.55	0.22	69.94	0.32
Rhone	965	0.63	0.26	69.04	0.38
Rift Valley	157	0.92	1.24	213.07	0.58
Rio Balsas	448	0.86	0.79	144.45	0.54
Rio Grande - Bravo	2,698	1.16	1.79	327.31	0.55
Rio Lerma	799	0.80	1.15	210.68	0.54
Rio Verde	346	0.75	0.31	54.97	0.57
Russia, South East Coast	69	0.52	0.09	17.96	0.48
Sabarmati	2,392	0.92	0.93	126.39	0.74
Salinas Grandes	182	1.03	0.05	8.99	0.54
Salween	411	0.79	0.19	34.13	0.54

Sao Francisco	916	0.72	2.63	759.84	0.35
Saskatchewan - Nelson	11,361	0.72	4.25	927.95	0.46
Scandinavia, North Coast	873	0.66	3.92	887.29	0.44
Scheldt	350	0.60	0.00	0.63	0.56
Scotland	466	0.53	0.18	54.56	0.34
Seine	612	0.69	0.07	11.32	0.59
Senegal	66	0.87	0.41	121.95	0.34
Shebelli - Juba	423	0.92	0.16	24.36	0.66
Sittang	114	0.77	0.81	117.61	0.69
South Africa, South Coast	7,959	0.68	0.44	150.36	0.30
South Africa, West Coast	2,766	0.72	0.06	14.29	0.39
South America, Colorado	1,467	1.21	0.63	81.72	0.78
South Argentina, South Atlantic Coast	114	0.75	0.13	21.08	0.61
South Chile, Pacific Coast	1,490	0.76	0.73	218.69	0.33
South China Sea Coast	3,148	0.60	0.50	147.51	0.34
Southern Central America	457	1.08	1.12	157.63	0.71
Spain - Portugal, Atlantic Coast	4,572	0.98	0.42	90.72	0.47
Spain, South and East Coast	6,120	0.89	0.48	92.65	0.52
Sri Lanka	2,405	0.82	0.50	101.77	0.49
St John	292	0.49	0.11	31.43	0.35
St Lawrence	9,727	0.70	7.55	1,778.50	0.42
Sumatra	318	1.06	0.68	53.98	1.25
Sweden	891	0.61	1.27	292.73	0.43
Syr Darya	783	0.72	2.95	591.41	0.50
Tagus	1,576	0.90	0.56	137.62	0.41
Taiwan	680	0.93	0.19	23.39	0.82
Tapti	1,114	0.81	0.94	156.91	0.60
Tarim Interior	594	0.97	1.20	125.33	0.96
Tasmania	815	1.04	1.83	223.38	0.82
Tiber	481	0.78	0.06	9.40	0.62
Tigris - Euphrates	1,089	0.87	10.36	2,363.37	0.44
Tocantins	1,344	0.68	6.96	1,217.99	0.57
United States, North Atlantic Coast	8,518	0.46	0.65	196.40	0.33
Ural	224	0.52	0.17	56.33	0.31
Uruguay - Brazil, South Atlantic Coast	7,916	0.78	2.10	407.95	0.52
Viet Nam, Coast	959	0.75	1.58	266.93	0.59
Volga	3,234	0.56	7.77	2,032.44	0.38
Volta	544	0.79	7.77	1,672.54	0.46
Wisla	3,583	0.60	0.11	33.27	0.34
Xun Jiang	8,924	0.64	4.18	1,056.68	0.40
Yangtze	55,171	0.42	16.81	4,182.75	0.40
Yasai	846	0.88	0.56	109.92	0.51
Yenisei	53	0.57	11.65	4,249.61	0.27
Yucatan Peninsula	78	1.10	0.01	1.47	0.67
Zambezi	2,212	0.81	11.32	2,667.56	0.42
Ziya He, Interior	1,494	0.83	1.35	325.07	0.41

Table 5.

Statistics on reservoir capacity and sedimentation rate in different climate zones.

Climate zone	Reservoir number	Annual sedimentation rate (%)	Annual total sediments (10^8 m^3)	Reservoir storage capacity (10^8 m^3)	Annual capacity loss rate (%)
Arid	10,183	1.01	16.93	4,354.08	0.39
Semiarid	110,606	0.87	60.79	12,867.95	0.47
Dry subhumid	72,409	0.80	57.29	11,079.83	0.52
Humid	362,762	0.67	226.14	47,470.98	0.48

Table 6.

Statistics on reservoir capacity and sedimentation rate in different area ranges.

Area (km^2)	Reservoir number	Annual sedimentation rate (%)	Annual total sediments (10^8 m^3)	Reservoir storage capacity (10^8 m^3)	Annual capacity loss rate (%)
0.001 – 0.1	432,914	0.77	7.41	977.23	0.76
0.1 – 1	97,387	0.62	16.67	2,526.21	0.66
1 – 10	21,317	0.59	40.90	7,076.40	0.58
10 – 100	3,781	0.51	90.55	17,422.51	0.52
>100	561	0.50	205.62	47,770.49	0.43

Table 7.

Statistics on reservoir capacity and sedimentation rate in major biomes zones (biomes zones with fewer than 1,000 reservoirs excluded).

Major biomes	Reservoir number	Annual sedimentation rate (%)	Annual total sediments (10^8 m^3)	Reservoir storage capacity (10^8 m^3)	Annual capacity loss rate (%)
Boreal forests/Taiga	3,306	0.63	41.01	10,380.10	0.40
Deserts & Xeric Shrublands	27,783	0.98	22.56	5,668.54	0.40
Flooded Grasslands & Savannas	1,495	0.74	2.05	291.19	0.71
Mangroves	1,493	0.91	0.05	7.03	0.76
Mediterranean Forests, Woodlands & Scrub	45,035	0.90	13.02	2,719.65	0.48
Montane Grasslands & Shrublands	7,270	0.88	6.72	984.95	0.68
Temperate Broadleaf & Mixed Forests	182,524	0.60	59.43	13,269.43	0.45
Temperate Conifer Forests	15,501	0.75	22.14	4,317.17	0.51
Temperate Grasslands, Savannas & Shrublands	116,652	0.80	37.22	7,826.87	0.48
Tropical & Subtropical Coniferous Forests	2,233	0.98	3.27	448.84	0.73
Tropical & Subtropical Dry Broadleaf Forests	38,914	0.78	22.33	4,322.53	0.52
Tropical & Subtropical Grasslands, Savannas & Shrublands	34,056	0.80	53.61	10,415.03	0.51
Tropical & Subtropical Moist Broadleaf Forests	77,850	0.68	73.22	14,348.19	0.51
Tundra	590	0.64	2.72	494.88	0.55

Table 8.

Statistics on reservoir capacity and sedimentation rate in different Köppen climate types (climate zone with fewer than 1,000 reservoirs excluded).

Köppen climate types	Reservoir number	Annual sedimentation rate (%)	Annual total sediments (10^8 m^3)	Reservoir storage capacity (10^8 m^3)	Annual capacity loss rate (%)
Af	3,149	1.01	7.47	1,494.16	0.50
Am	7,782	0.90	24.02	4,095.79	0.59
As	45,999	0.78	70.74	13,207.40	0.54
Aw	12,150	1.00	10.62	3,402.92	0.31
BSh	8,343	1.08	8.89	1,797.95	0.49
BSk	31,743	0.87	24.35	4,317.24	0.56
BWh	49,263	0.87	21.88	4,257.19	0.51
BWk	22,219	0.90	14.24	3,161.90	0.45
Cfa	10,890	0.95	3.67	692.32	0.53
Cfc	35,139	0.65	28.03	5,569.67	0.50
Csa	12,031	0.83	3.05	493.55	0.62
Csc	172,650	0.62	40.67	9,218.94	0.44
Cwa	20,902	0.71	5.76	1,164.27	0.49
Dfa	1,419	0.85	2.53	453.35	0.56
Dfd	14,934	0.70	6.36	1,678.88	0.38
Dsa	2,123	0.72	8.16	1,834.96	0.44
Dsd	36,332	0.77	8.22	1,820.11	0.45
Dwa	62,898	0.61	29.65	8,290.84	0.36
Dwb	3,303	0.64	31.89	7,135.01	0.45
Dwd	1,485	0.76	1.45	230.31	0.63

Table 9.

Statistics on costs for sediment removal measures in different counties.

Region	Country	Sediment removal methods	Mean cost($ per m³)	Source
Mrica Banjarnegara	Indonesia	flushing	1.48	https://doi.org/10.1080/10402381.2024.2319590
Not provided	United States	flushing	1.48	https://doi.org/10.1029/WR023i008p01443
Shihmen Reservoir	China	flushing	1.87	https://doi.org/10.3390/w10081034
Not provided	Uzbekistan	flushing	2.00	https://doi.org/10.1016/S1872-1990(08)80008-6
Barra-Vagueira	Portugal	flushing	2.18	https://doi.org/10.3390/jmse10121906
Not provided	India	flushing	2.41	https://www.business-standard.com/article/specials/silt-removal-in-dvc-reservoirs-to-cost-over-rs-3500-crore-197032401048_1.html
Nqweba Dam, EC	South Africa	flushing	2.74	https://www.researchgate.net/publication/355985086
Campsdrift, Pietermaritzburg	South Africa	flushing	2.91	https://www.researchgate.net/publication/355985086
Nam Kong 1	Laos	flushing	3.00	https://doi.org/10.1029/2020WR028351
Danube River Basin	Bulgaria	flushing	3.27	https://doi.org/10.1016/j.jclepro.2023.140183
Mengjin Reservoir	China	flushing	3.54	https://doi.org/10.7666/d.Y3265817
Danube River Basin	Romania	flushing	3.82	https://doi.org/10.1016/j.jclepro.2023.140183
Galati	Romania	flushing	3.82	https://doi.org/10.1016/j.jclepro.2023.140183
Oliphantskop Dam, KZN	South Africa	flushing	4.14	https://www.researchgate.net/publication/355985086
Xiagou Reservoir	China	flushing	4.66	https://doi.org/10.3880/j.issn.1006-7647.2024.04.008
Not provided	Finland	flushing	5.45	https://doi.org/10.3390/su13169349
Cogswell Reservoir	United States	mechanical dredging	5.60	https://doi.org/10.1002/2013EF000184
Tuttle Creek Lake watershed	United States	mechanical dredging	8.21	https://doi.org/10.1080/10402381.2013.814184
San Clemente Dam	United States	mechanical dredging	10.46	https://doi.org/10.1080/10402381.2013.814184
Limburg	Netherlands	mechanical dredging	11.99	https://doi.org/10.1002/0470859202.ch31
Veľké Kozmálovce Reservoir	Slovakia	mechanical dredging	16.35	https://doi.org/10.1016/j.jclepro.2023.140183
Not provided	Spain	mechanical dredging	10.90-21.80	https://doi.org/10.1065/jss2007.08.244

Auvergne-Rhône-Alpes	France	mechanical dredging	18.53-21.80	https://doi.org/10.1016/j.jclepro.2023.140183
Mlýnka River	Czechia	mechanical dredging	21.80	https://doi.org/10.1016/j.jclepro.2023.140183
Normandy	France	mechanical dredging	21.80	https://doi.org/10.1016/j.landusepol.2021.105541
Bourgogne-Franche-Comté	France	mechanical dredging	21.8027.25	https://doi.org/10.1016/j.jclepro.2023.140183
Not provided	Italy	mechanical dredging	30.52	https://doi.org/10.1016/j.jclepro.2023.140183

Table 10.

Statistical summary of reservoir sedimentation hotspot regions. The spatial locations of these hotspots are shown in Extended Data Fig. 8. Abbreviations for Köppen zones and biome zones follow those used in Fig. 5 and Fig. 6.

Hot spot region	Region area (10^6 km^2)	Reservoir number	Reservoir area (km^2)	Reservoir storage capacity (10^8 m^3)	Annual sedimentation rate (%)	Major Köppen Zone	Major Biomes Zone
Western USA	2.21	3,149	6,155.82	6,155.82	1.12	BWh, BSk	DXS
Caribbean	0.99	7,782	2,087.16	418.84	1.02	Aw, Af	TSMBF
Andean mountains	2.89	45,999	4,854.14	788.89	0.97	BWk	MGS
Namibia	0.96	12,150	567.87	52.97	1.44	BWh	DXS
East Africa	2.42	8,343	4,310.91	1,238.19	0.99	BSh, Aw	TSGSS
Red Sea	0.50	31,743	159.36	26.01	1.00	BWh	DXS
Middle East	0.81	49,263	2,590.36	757.32	0.91	BSk, Csa	TBMF
Indus river basin	1.75	22,219	3,788.61	1,096.36	0.96	BWh	DXS
Himalayas	2.00	10,890	2,311.34	1,012.63	0.91	ET, Cwa	MGS
Tarim	0.57	35,139	1,548.69	108.71	0.91	DXS	DXS
Yellow river basin	0.71	12,031	1,937.12	301.19	1.09	BSk	MGS
Philippines	0.25	172,650	536.86	92.49	1.10	Af, Am	TSMBF
Indonesia	1.03	20,902	1,748.59	784.72	1.02	Af	TSMBF
Western AU	0.56	1,419	178.67	18.88	1.22	BWh, Bsh	MFWS, DXS
Southeastern AU	1.09	14,934	2,380.51	423.86	0.98	BSh, Cfb	FGS, TBMF
New Zealand	0.22	2,123	346.60	60.50	0.88	Cfb	TBMF

Table 11.

The source, unit, category, resolution, time coverage and reference of global datasets regarding variables for machine learning modeling used in this study. The underlined indicators are not used for reservoir capacity modeling but are applied exclusively for prediction of reservoir sedimentation.

Category	Statistics zone	Long Name	Short Name	Spatial	Time	Data Source	Source link
Reservoir location and morphometry	Reservoir extent	Longitude	Longitude	30 m	Current	GREI	Direct calculation
	Reservoir extent	Latitude	Latitude	30 m	Current	GREI	Direct calculation
	Reservoir extent	Area	Area	30 m	Current	GREI	Direct calculation
	Reservoir extent	Perimeter	Perimeter	30 m	Current	GREI	Direct calculation
	Reservoir extent	Shoreline shape index	ShaIndex	30 m	Current	GREI	Direct calculation
	Reservoir extent	Shoreline roundness	Roundness	30 m	Current	GREI	Direct calculation
	Reservoir extent	Area circumference ratio	AreaRatio	30 m	Current	GREI	Direct calculation
	Reservoir extent	Continent	Continent	30 m	Current	GREI	Direct calculation
	Reservoir extent	Basin	Basin	410 m	Current	HydroBASINS	https://www.hydrosheds.org/products/hydrobasins
Geomorphology, lithology	Reservoir extent	Lithology type	Lithology	250 m	Current	USGS global ecosystem map	https://zenodo.org/records/1464846#.YoXUVOhBw2w
	Reservoir extent	Landform type	Landform	250 m	Current	USGS global ecosystem map	Same as above
	Reservoir extent	Elevation	Elevation	90 m	Current	MERIT DEM	https://zenodo.org/record/1447210#.YvX4HtBByHs
	Reservoir buffer zone	Elevation difference	EleDiff	90 m	Current	MERIT DEM	Same as above
	Reservoir buffer zone	Slope	Slope	90 m	Current	MERIT DEM	Same as above
	Reservoir buffer zone	Curvature	Curvature	90 m	Current	MERIT DEM	Same as above
	Reservoir buffer zone	Topographic wetness index	TWI	90 m	Current	MERIT DEM	Same as above
	Reservoir buffer zone	Permeability	Permeability	1 km	Current	GLHYMPS	https://agupubs.onlinelibrary.wiley.com/doi/full/10.1002/2014gl059856
	Reservoir buffer zone	Porosity	Porosity	1 km	Current	GLHYMPS	Same as above
	Reservoir catchment	<u>Catchment slope</u>	CatSlope	90 m	Current	MERIT DEM	https://zenodo.org/record/1447210#.YvX4HtBByHs
Soil	Reservoir extent	Soil type	SoilType	900 m	Current	Harmonized World Soil Database v 1.2	https://www.fao.org/soils-portal/data-hub/soil-maps-and-databases/harmonized-world-soil-database-v12/en/
	Reservoir catchment	<u>Rainfall erosivity</u>	R-factor	1 km	Current	ESDAC	https://esdac.jrc.ec.europa.eu/content/gloreda
	Reservoir catchment	<u>Soil erodibility</u>	K-factor	1 km	Current	ESDAC	https://esdac.jrc.ec.europa.eu/content/global-soil-erodibility
	Reservoir catchment	<u>Soil erosion</u>	SoilErosion	1 km	Current	ESDAC	https://esdac.jrc.ec.europa.eu/content/global-soil-erosion
	Reservoir buffer zone	Sand content	Sand	250 m	Current	SoilGrids	https://www.isric.org/explore/soilgrids
	Reservoir buffer zone	Silt content	Silt	250 m	Current	SoilGrids	Same as above
	Reservoir buffer zone	Clay content	Clay	250 m	Current	SoilGrids	Same as above
Climate	Reservoir catchment	Temperature	Temp	90 m	1980-2020	ERA5-Land	https://cds.climate.copernicus.eu/cdsapp#!/dataset/reanalysis-era5-land?tab=overview
	Reservoir catchment	Precipitation	Pre	90 m	1980-2020	ERA5-Land	Same as above
	Reservoir catchment	Evapotranspiration	Eva	90 m	1980-2020	ERA5-Land	Same as above
	Reservoir catchment	Wind speed	Wind	90 m	1980-2020	ERA5-Land	Same as above

	Reservoir catchment	Aridity Index	Aridity	90 m	1970-2000	ai_et0	https://figshare.com/articles/dataset/Global_Aridity_Index_and_Potential_Evapotranspiration_ET0_Climate_Database_v2/7504448/3
	Reservoir extent	Climate type	ClimateType	1 km	Current	GloH20	https://www.gloh2o.org/koppen/
Hydrology	Reservoir extent	River order	RivOrder	90 m	Current	MERIT DEM	https://zenodo.org/record/1447210#.YvX4HtBByHs
	Reservoir extent	River slope	RivSlope	90 m	Current	MERIT DEM	Same as above
	Reservoir extent	River runoff	RivRunoff	90 m	1980-2019	GRFR	https://www.tpdc.ac.cn/zh-hans/data/89c36e43-3690-4e5b-bf0a-19d057876dfe/?q=
	Reservoir extent	<u>River sediment</u>	RivSediment	2,067 largest river	1990-2019	ECohen_2022	https://arcg.is/1m5W4m0
	Reservoir extent	<u>Flood event</u>	Flood	0.05°	1980-2019	GRFR	https://www.tpdc.ac.cn/zh-hans/data/89c36e43-3690-4e5b-bf0a-19d057876dfe/?q=
	Reservoir catchment	Catchment area	CatArea	90 m	Current	Lake-TopoCat	https://essd.copernicus.org/articles/15/3483/2023/
	Reservoir catchment	<u>Recharge coefficient</u>	Recharge	90 m	Current	Lake-TopoCat	Same as above
	Reservoir catchment	Glacier-covered region	GlaCovered	90 m	Current	Jürgen_ Philip_2003	https://www.sciencedirect.com/science/article/pii/S0277379103001306#aep-section-id28
	Reservoir catchment	Endorheic basin	Endorheic	410 m	Current	HydroSHEDS	https://www.hydrosheds.org/
Land cover	Reservoir catchment	<u>Vegetation index</u>	NDVI	9 km	1982-2022	PKU GIMMS NDVI	https://essd.copernicus.org/articles/15/4181/2023/
	Reservoir catchment	<u>Bareland ratio</u>	Bare	90 m	1992-2020	PFT	https://catalogue.ceda.ac.uk/uuid/26a0f46c95ee4c29b5c650b129aab788
	Reservoir catchment	<u>Cropland ratio</u>	Cropland	90 m	1992-2020	PFT	Same as above
	Reservoir catchment	<u>Grass ratio</u>	Grass	90 m	1992-2020	PFT	Same as above
	Reservoir catchment	<u>Tree ratio</u>	Tree	90 m	1992-2020	PFT	Same as above
Human activities	Reservoir catchment	Impervious area	Lmp	30 m	1985-2018	FROM-GLC	https://data-starcloud.pcl.ac.cn/zh
	Reservoir catchment	Nighttime light	NTL	90 m	1992-2018	Li_Zhou_2020	https://www.nature.com/articles/s41597-020-0510-y#Sec8
	Reservoir catchment	Population density	Pop	1 km	2000, 2005, 2010, 2015, 2020	ESDAC	https://sedac.ciesin.columbia.edu/data/set/gpw-v4-population-density-rev11

Table 12.

Adopted experiments to determine the optimal machine learning prediction model and assess its robustness. In this study, we carried out comprehensive and multidimensional testing to select the best-performing machine learning model and systematically evaluate factors that might influence its stability. This rigorous approach ensures the model achieves high accuracy and reliability for global-scale predictions.

Type	Test objective	Results
Algorithm selection	Compare the accuracy of different machine learning models	See Figs. 23 and 24
Hyperparameters	Test the optimal hyperparameters of different machine learning models to improve their performances	See Table 13
Variable selection	Test whether selecting variables with high importance can improve model accuracy	See Table 14
Sample selection	Test whether the high concentration of sedimentation samples in the China region impacts prediction results	See Table 15
	To evaluate the spatial generalizability of the model by using leave-region-out validation	See Figs. 25, 26
	Evaluate whether the samples are representative across different predictor variables	See Fig. 28
	Evaluated the model performance when trained separately on groups stratified by reservoir size and climate zones.	See Table 16 and 17
Scale selection	Test the consistency between global-scale and national-scale model predictions	See Fig. 27

Table 13.

Candidate values for hyperparameters of the XGBoost model.

The hyperparameters to be determined	Candidate value
n_estimators	100
max_depth	40
min_child_weight	20
learning_rate	0.05
subsample	1
colsample_bytree	0.5
gamma	0

Table 14.

The influence of variable selection on annual sedimentation rate prediction. By selecting the most important factors, as identified by their SHAP rankings, the present study aimed to test the effectiveness of variable importance in enhancing model performance.

Variable selection	MAE (%)	RMSE (%)
Top 10	0.34	0.67
Top 15	0.33	0.66
Top 20	0.33	0.67
All	0.33	0.66

Table 15.

The influence of sample selection ratio on annual sedimentation rate prediction. The sample selection ratio is defined as the ratio of samples from regions outside China to those within China. Given the higher concentration of reservoir sedimentation samples in the China region in this study, this experiment aims to primarily evaluate the impact of spatially uneven sample distribution on model accuracy.

Sample selection ratio	MAE (%)	RMSE (%)
0.25	0.38	0.71
0.5	0.38	0.71
1	0.37	0.66
1.5	0.38	0.70
2	0.36	0.72
2.5	0.37	0.71
3	0.34	0.66

Table 16.

Stratified validation of sedimentation rate predictions across four reservoir size classes

Area (km^2)	Training number	Test number	MAE (%)	RMSE (%)
<0.1	2,063	884	0.29	0.59
0.1–1	1,335	572	0.35	0.68
1–10	576	247	0.41	0.75
>10	319	137	0.40	0.86

Table 17.

Stratified validation of reservoir sedimentation rate predictions based on climate zone categories.

Climate zone	Training number	Test number	MAE (%)	RMSE (%)
Arid	51	22	0.71	1.01
Semiarid	403	173	0.61	1.08
Dry subhumid	229	98	0.55	0.99
Humid	3,610	1,547	0.28	0.56